Cell Reports
Medicine

Article

A longitudinal single-cell and spatial multiomic atlas of pediatric high-grade glioma

Graphical abstract

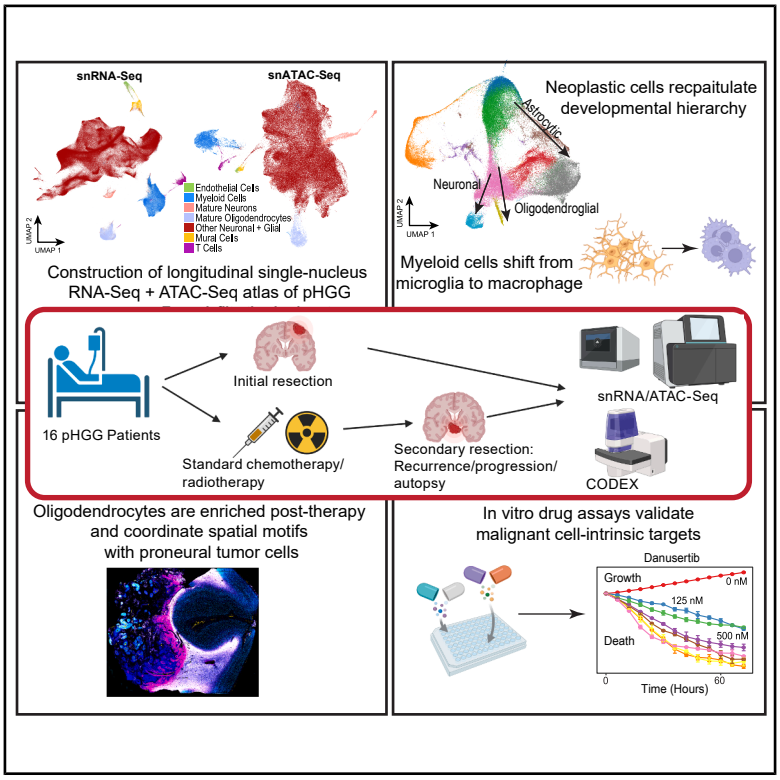

Highlights

- A multiomic atlas defines pHGG neoplastic cell states across molecular subtypes
- Oligodendrocytes increase post-therapy and coordinate with tumor cells
- Myeloid cells shift from microglial to macrophage phenotypes
- Interferon-mediated neuroactive signaling pathways are upregulated over time

Authors

Jonathan H. Sussman, Derek A. Oldridge, Wenbao Yu, ..., Thomas De Raedt, Kristina Cole, Kai Tan

Correspondence

tank1@chop.edu

In brief

Sussman et al. present a longitudinal multiomic study of pediatric high-grade glioma, integrating single-nucleus transcriptomics, epigenomics, genomics, and spatial proteomics across disease progression. This work characterizes malignant cell states, therapy-associated neoplastic and immune programs, and spatial tumor-glial interactions, providing a reference for pediatric brain tumor biology.

Sussman et al., 2026, Cell Reports Medicine 7, 102766
May 19, 2026
https://doi.org/10.1016/j.xcrm.2026.102766

CellPress

Cell Reports Medicine

CellPress
OPEN ACCESS

Article

A longitudinal single-cell and spatial multiomic atlas of pediatric high-grade glioma

Jonathan H. Sussman,[1,2,15] Derek A. Oldridge,[3,4,15] Wenbao Yu,[5,6,15] Chia-Hui Chen,[5] Abigail M. Zellmer,[4] Jiazhen Rong,[2,7] Arianne Parvaresh-Rizi,[8] Anusha Thadi,[5] Austin Yang,[5] Joseph S. Tumulty,[5] Barbara Xiong,[1,2] David W. Wu,[1,2] Yusha Sun,[1,9] Shovik Bandyopadhyay,[1,10] Jason Xu,[1,2] Stephanie Brosius,[5] Una Yamamoto Barkardottir,[5] Isabelle Seka,[5] Kyung Jin Ahn,[5] Omar Elghawy,[11] Amy E. Baxter,[4] Mateusz P. Koptyra,[12] Rami S. Vanguri,[4] Stephanie McGrory,[5] Phillip B. Storm,[12] Nduka M. Amankulor,[13] Mariarita Santi,[3] Angela N. Viaene,[3] Nancy Zhang,[7] Thomas De Raedt,[3,5] Kristina Cole,[5,6] and Kai Tan[5,6,14,16,*]

[1]Medical Scientist Training Program, Perelman School of Medicine, University of Pennsylvania, Philadelphia, PA, USA
[2]Graduate Group in Genomics and Computational Biology, Perelman School of Medicine, University of Pennsylvania, Philadelphia, PA, USA
[3]Department of Pathology and Laboratory Medicine, Perelman School of Medicine at the University of Pennsylvania, Philadelphia, PA, USA
[4]Center for Computational and Genomic Medicine, Children's Hospital of Philadelphia, Philadelphia, PA, USA
[5]Center for Childhood Cancer Research, Children's Hospital of Philadelphia, Philadelphia, PA, USA
[6]Department of Pediatrics, University of Pennsylvania Perelman School of Medicine, Philadelphia, PA, USA
[7]Department of Statistics and Data Science, University of Pennsylvania, Philadelphia, PA, USA
[8]Department of Medicine, Warren Alpert Medical School of Brown University, Providence, RI, USA
[9]Neuroscience Graduate Group, Perelman School of Medicine, University of Pennsylvania, Philadelphia, PA, USA
[10]Cellular and Molecular Biology Graduate Group, Perelman School of Medicine, University of Pennsylvania, Philadelphia, PA, USA
[11]Department of General Internal Medicine, University of Pennsylvania, Philadelphia, PA, USA
[12]Department of Neurosurgery, Children's Hospital of Philadelphia, Philadelphia, PA, USA
[13]Department of Neurosurgery, Perelman School of Medicine, Philadelphia, PA, USA
[14]Center for Single Cell Biology, Children's Hospital of Philadelphia, Philadelphia, PA, USA
[15]These authors contributed equally
[16]Lead contact
*Correspondence: tank1@chop.edu
https://doi.org/10.1016/j.xcrm.2026.102766

SUMMARY

Pediatric high-grade glioma (pHGG) is an incurable central nervous system malignancy that is a leading cause of pediatric cancer death. While pHGG shares many similarities with adult glioma, it comprises distinct disease entities. In this study, we longitudinally profile a molecularly diverse cohort of 16 pHGG patients through single-nucleus RNA and ATAC sequencing, whole-genome sequencing, and CODEX spatial proteomics to capture the evolution of neoplastic and microenvironmental features during disease progression and treatment. We define a set of core pHGG neoplastic cell states and observe differential tumor-myeloid interactions between malignant cell phenotypes. We find that essential neuromodulators and the interferon response are upregulated post-therapy, implicating them as malignant cell-intrinsic targets. We observe an increase in oligodendrocytes upon progression and that they coordinate spatial motifs with proneural tumor cells. This multiomic atlas of longitudinal pHGG captures features of therapy response and provides a scalable reference for the study of pediatric brain tumors.

INTRODUCTION

Pediatric high-grade glioma (pHGG) is a devastating brain malignancy accounting for approximately 11% of central nervous system (CNS) tumors in children from infants to adolescents.[1] Although the incidence of pHGG is relatively low (1.78 per 100,000 population), it holds an exceptionally dismal prognosis, with a median overall survival of 10–18 months.[2] Despite decades of research and over 1,500 glioma clinical trials,[3] there remains no cure for pHGG. Standard therapy includes maximal safe resection, high-dose radiotherapy, and chemotherapy, yet this multimodal therapy only increases the overall survival on the order of months.[4] Although childhood and adult HGG, including glioblastoma multiforme (GBM), share many histopathological and clinical features, the advent of genomic, transcriptomic, and epigenomic profiling has led to revised classifications within the current 2021 World Health Organization (WHO) classification of CNS tumors.[2,5–10] It is now recognized that pHGG can be further categorized through methylation profiling into "pediatric-type" diffuse HGG subclasses (e.g., diffuse midline glioma, K27M-altered). Moreover, a patient in the pediatric age range may present with an "adult-type" diffuse glioma (e.g., astrocytoma, IDH-mutant).[5] The H3K27M mutation occurs frequently in tumors arising in the brainstem and other midline structures

including the thalamus and cerebellum, while the H3G34R/V mutation is found most frequently in adolescent pHGGs of the cerebral cortex.[2,6]

Recent advances in single-cell multiomics and spatial profiling have greatly informed our understanding of the intra-tumoral and inter-tumoral heterogeneity of adult and pediatric brain tumors.[11–28] Collectively, these studies have identified patterns of neoplastic cell differentiation states and metabolic programs, proposed detailed models for tumor initiation and oncogenesis, characterized the tumor immune microenvironment (TIME), and identified actionable avenues for targeted chemotherapeutic and immunotherapeutic strategies. Importantly, recent studies using bulk and single-cell transcriptomics have established the paradigm that glioma subtypes, and CNS tumors more broadly, are similarly characterized by derangements in neurodevelopmental differentiation and immunosuppressive microenvironmental features.[11,19,29–34] However, current single-cell analysis of pHGG[11,15,16,19,21,24,35] primarily focuses on diffuse midline glioma, and the molecular and microenvironmental changes of pHGG progression under therapy across subtypes have not been thoroughly evaluated. In order to identify common features of pHGG, we present an integrated multimodal atlas of matched primary-recurrent patient specimens from 16 patients across histologic and molecular subtypes using single-nucleus transcriptomic and chromatin accessibility sequencing and spatial proteomics. This atlas first establishes a reference of malignant and microenvironmental phenotypes in pHGG, which then serves as a foundation for interrogating longitudinal transcriptional and immunological changes within the paired patient-level data.

RESULTS

Single-cell profiling of longitudinal pHGG specimens

We profiled pHGG samples obtained through the Children's Brain Tumor Network (CBTN)[36] from 16 patients across therapeutic time points via single-nucleus RNA sequencing (snRNA-seq) (15 pairs) and single-nucleus assay for transposase-accessible chromatin using sequencing (snATAC-seq) (11 pairs) (Figures 1A–1C). The inclusion criterion included patients diagnosed histologically with a high-grade glioma under the age of 18 years who were prospectively enrolled for subsequent profiling at recurrence, progression, or autopsy. All patients received radiotherapy and surgical resection, and some received pharmacological treatment including temozolomide, immunotherapy (e.g., pembrolizumab), and cytotoxic chemotherapy (Figure S1A; Tables S1 and S2). Patients in the cohort were aged 4–18 years at diagnosis, had a male-to-female ratio of 2.2, and exhibited tumors with a range of genomic alterations (Figures S1B–S1D; Table S3). The tumor specimens were resected from multiple anatomic locations including cortical lobes and midline structures (thalamus and cerebellum). The cohort included three H3K27M-mutated cases, two H3G34R/V-mutated cases, and one pediatric IDH1-mutated case; the remainder were IDH1/H3-wildtype (WT) (Figure 1D). Methylation profiling classified 12 of the patients within the "pediatric-type diffuse high-grade glioma" family, two patients within the "adult-type diffuse glioma" family, and two within other categories (Table S2). Collectively, over 400,000 cells were profiled via snRNA-seq, and over 110,000 cells were profiled via snATAC-seq after quality assessment and filtering, capturing a mean of 2,280 genes and 19,094 unique chromatin fragments per cell, respectively (Figure S2). Post-therapy time points (non-treatment naive) were further delineated as progressive/recurrence or autopsy, depending on whether samples were obtained through a secondary resection or were collected post-mortem, and we confirmed that there were no systematic differences in data quality between these collection methods (Figures S3A–S3C). Samples were integrated to remove batch effects, and cell types were annotated (Figures S3 and S4). We captured the major cell types present in gliomas, including normal mature neurons and oligodendrocytes, myeloid cells (macrophages/microglia), T cells, endothelial cells, mural cells, and a diverse population that we have termed "other neuronal and glial cells," including a mix of inferred neoplastic and non-neoplastic subpopulations (Figures 1B and 1C; Table S4). There was significant heterogeneity between patients and time points (Figures 1D, S2B, S2C, and S2I–S2K). Notably, the majority of mural cells were captured within two patients, and T cells were captured largely in a single patient (Figure 1D). Examining the longitudinal shifts in cell-type composition in the snRNA-seq data revealed a significant increase in non-neoplastic oligodendrocytes and mature neurons within patient-matched pairs (Figures 1E and S3G). Oligodendrocytes were concordantly enriched post-therapy in the snATAC-seq data (Figure 1F), consistent with prior observations in adult glioblastoma multiforme (GBM).[22,26]

Pediatric gliomas exhibit distinct neoplastic cell states

We sought to characterize the neoplastic cell compartment and assess how these cell states change during progression and therapy. To that end, we identified putative neoplastic cells via copy number variation (CNV) inference (Figure S5) and found that the proportion of malignant cells was significantly decreased in the post-therapy time point (Figure S6A). Then, we reintegrated these populations (Figures S6B–S6D) and identified a set of core pHGG malignant cell states via unsupervised clustering of the integrated data. We annotated these cell states based on their differentially expressed genes and pathways, relative expression of published glioma cell state signatures derived from H3K27M-altered[19] and IDH/H3-WT[11] adult and pediatric HGG, and projection to a reference map of the developing fetal brain, derived from the telencephalon and forebrain at 13–21 weeks (Figures 2A–2G and S6E–S6I; Tables S5 and S6). First, we identified a mesenchymal (MES)-like state that expressed established mesenchymal marker genes (e.g., *CD44*, *VIM*, *ANXA1*, and *NDRG1*) and angiogenesis genes (e.g., *VEGFA*) and was enriched in hypoxia response signatures (Figures 2D and 2E). Moreover, we observed that while mesenchymal cells were most hypoxic, there was a wide range of variation between samples, even within individual cell states (Figure 2H). Interestingly, while the mesenchymal cell state has only recently been identified in H3K27M-mutant glioma,[19] which these findings further support, we observed a low-frequency MES-like state in our single pediatric IDH-mutant glioma case (Figure 2C). Next, we identified a population with high expression of both previously

CellPress
OPEN ACCESS

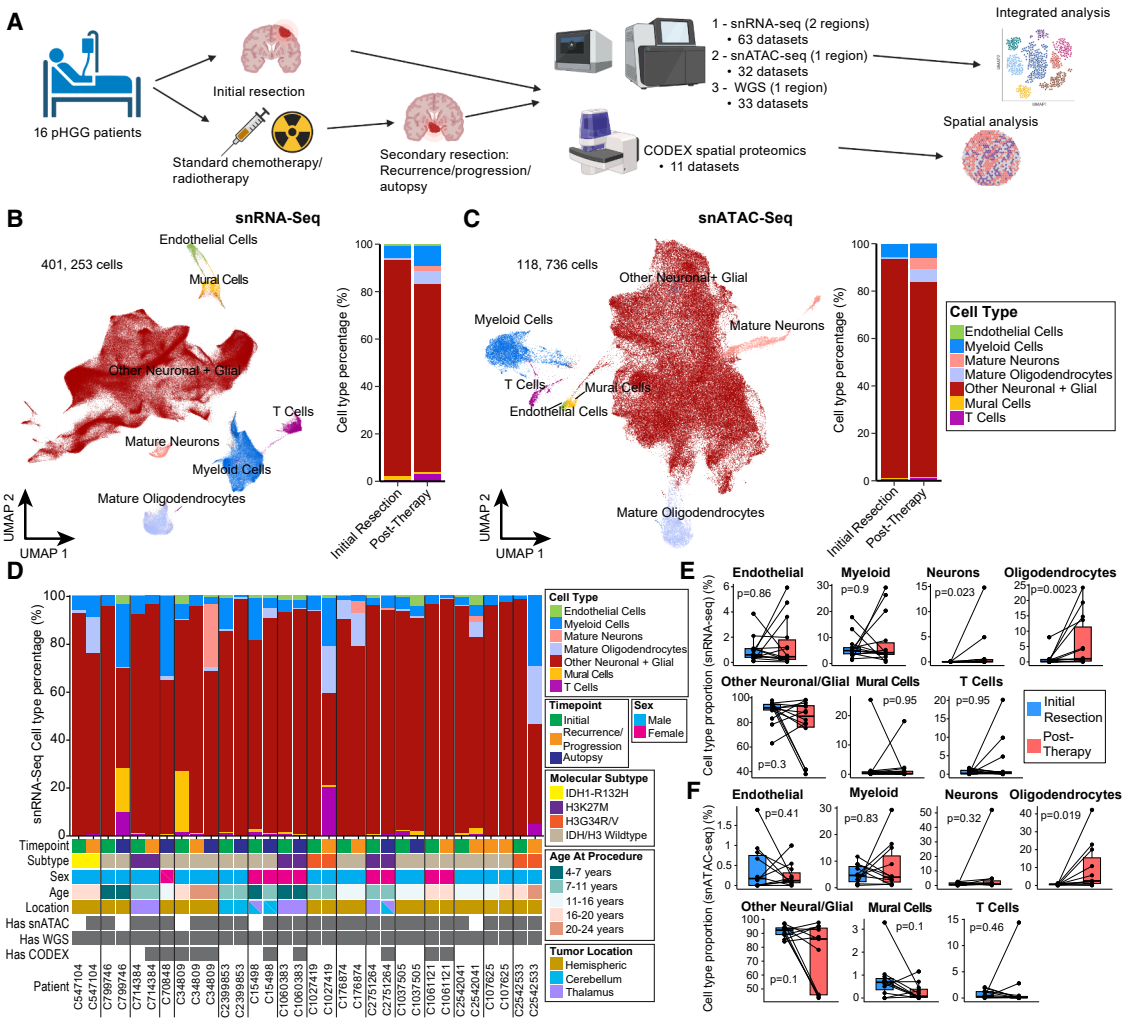

Figure 1. Longitudinal single-cell RNA and ATAC atlas of pediatric high-grade glioma (pHGG)

(A) Overview of the multiomics studies on patient-matched longitudinal pHGG specimens.

(B and C) Uniform manifold approximation and projection (UMAP) of (B) snRNA-seq data (401,253 cells) and (C) snATAC-seq data (118,736 cells) annotated by major cell type category (left) and stacked bar plot of cell-type proportions across dataset comparing initially resected pHGG samples with post-therapy samples.

(D) Cell-type proportions in snRNA-seq data across each patient and therapeutic time point, along with a summary of patient demographics and molecular subtype.

(E and F) Shifts in cell-type proportions for each patient between initial resection and post-therapy time points in (E) snRNA-seq (n = 14 initial/post-therapy paired samples) and (F) snATAC-seq (n = 11 paired samples). Post-therapy samples were merged for one patient with three longitudinal samples. A two-sided Wilcoxon signed-rank test for paired samples was used.

defined oligodendrocyte progenitor cell (OPC)-like and neural progenitor cell (NPC)-like gene signatures and enriched in neurodevelopmental and synapse-related pathways that we annotated as OPC/NPC-like (Figure 2E). Then, we identified two more differentiated populations: an oligodendrocyte (OC)-like state that expressed mature oligodendrocyte genes (e.g., *BCAS1* and *SIRT2*) and was enriched in an OC-like signature previously defined across H3K27M-mutant glioma[19] (Figures 2D and S6J) and a neuronal (NEU)-like state that highly expressed some NPC-like marker genes (e.g., *SOX4* and *CD24*), was enriched in neurotransmitter release pathways, and most closely resembled excitatory neurons when projected to the atlas of developing human fetal brain (Figure 2G). The NEU-like state was predominantly restricted to several IDH/H3-WT tumors (Figure 2C).

Then, we identified two populations with high expression of the astrocyte-defining marker *GFAP* that were most enriched in the astrocyte (AC)-like gene module established by Neftel et al.[11] in a cohort of IDH-WT adult (n = 20) and pediatric (n = 8) glioblastoma (GBM) (Figures 2D–2F). The first state projected partly onto glial progenitor cells, while the second state most closely resembled mature astrocytes; thus we termed these states GPC-like and AC-like, respectively. The GPC-like state was also relatively enriched for the Neftel OPC-like, but not Neftel NPC-like, gene module, consistent with a bipotent identity of GPCs (Figure 2G). To investigate the differentiation trajectory of

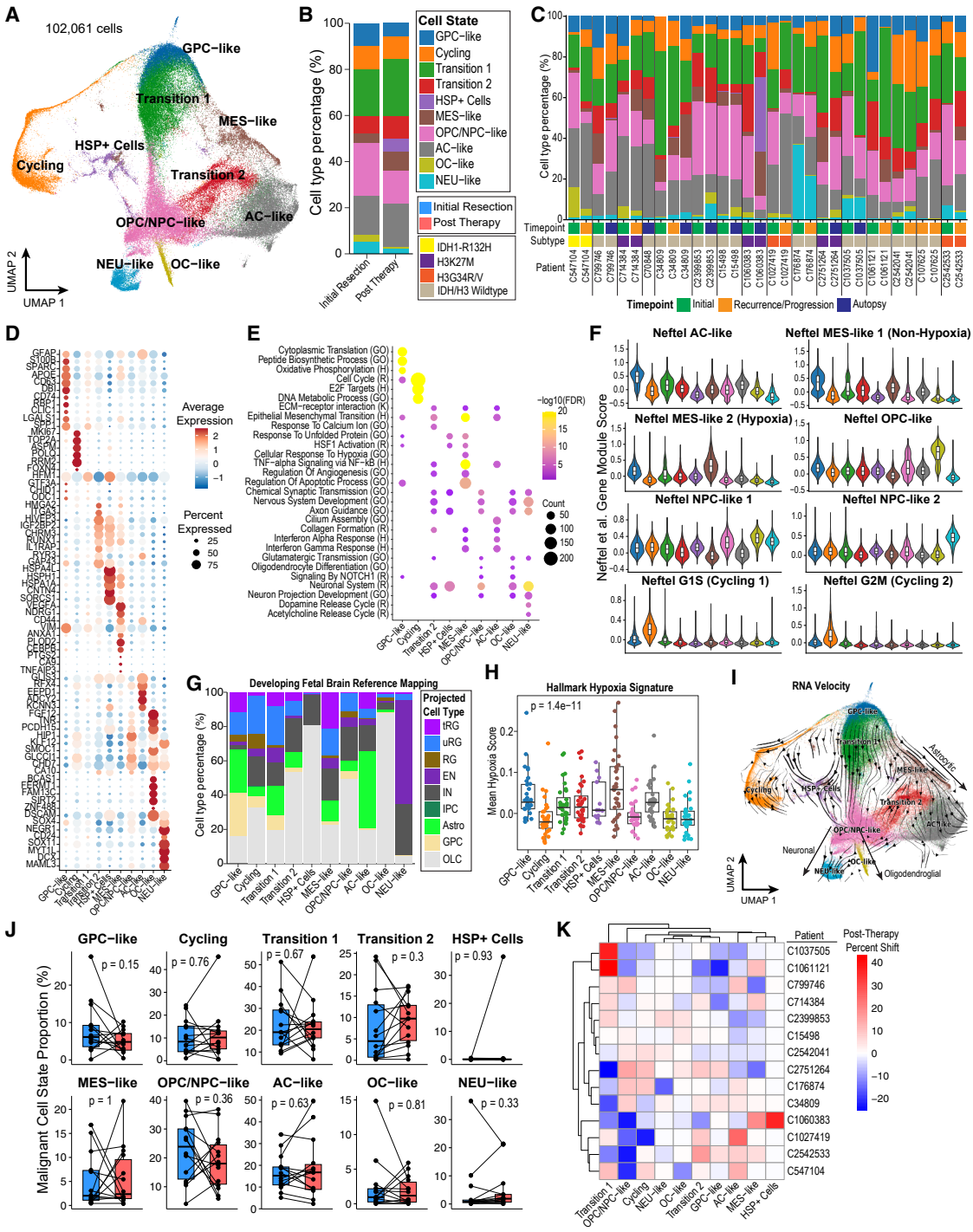

Figure 2. Transcriptional states of pHGG neoplastic cells

(A) UMAP projection of inferred neoplastic cells from snRNA-seq (102,061 cells) after integration and annotation of cell states; AC, astrocyte; GPC, glial progenitor cell; MES, mesenchymal; OC, oligodendrocyte; OPC, oligodendrocyte progenitor cell; NPC, neural progenitor cell; NEU, neural.

(B) Bar plot of cell-type proportions of neoplastic cells across dataset comparing initial resection and post-therapy samples.

(C) Neoplastic cell state proportions in snRNA-seq for each patient and therapeutic time point, along with the molecular subtype.

(D) Expression of representative differentially expressed genes across neoplastic cell states in snRNA-seq data.

(E) Pathway enrichment of top differentially expressed genes in each neoplastic cell state. Pathway database source is indicated in parentheses: GO, Gene Ontology terms; R, Reactome database; H, Hallmark database; K, KEGG database.

(F) Violin plots of gene signatures of GBM cell states (Neftel et al.)[11] for each pHGG cell state.

(legend continued on next page)

these cell states, we applied RNA velocity and pseudotime analyses across the neoplastic cells. These analyses revealed conserved hierarchical dynamics centered on the GPC-like state, with vector fields oriented toward astrocytic, oligodendroglial, and neuronal transcriptional programs, similar to patterns described in adult GBM.[13] While the representation of terminal states varied across individual patients and subtypes, the overall topological structure of these trajectories was reproducible (Figures 2I, S6K, and S7). Additionally, it indicated the presence of two transition states between the astrocytic/mesenchymal and proneural states with intermediate or mixed phenotypes as indicated by the gene and pathway analyses. Lastly, we identified a small, yet distinct, population of neoplastic cells found primarily in a single patient that was enriched in heat shock protein genes and annotated as HSP+ cells, likely representing an autopsy-induced phenotype, and a population of cycling cells that were shared across patients (Figures 2C–2E). Taken together, this establishes a robust atlas of single-nucleus transcriptomic neoplastic cell state that can be utilized for the reference mapping of both pediatric and adult HGG single-nucleus data (Figure S8).

The proportions of these cell states across samples were highly heterogeneous, with significant variation between patients and across time points (Figure 2C). However, examining neoplastic cell state proportions per patient revealed no significant shifts in cell-type composition across therapeutic time points, including on a sub-group analysis of IDH/H3-WT patients (Figures 2J and S6L). Rather, we observed heterogeneous patient-specific trajectories, analogous to what has recently been described in adult GBM (Figure 2K).[26] To validate our finding, we utilized our snRNA-seq reference to deconvolute a larger cohort of bulk RNA-seq data[37] of 201 pHGG patients including 23 paired samples. First, given our core pHGG cell populations, we identified significant differences in neoplastic cell states between subtypes: GPC-like and OC-like cells were most enriched in H3K27M glioma, cycling cells were most frequent in H3G34R/V glioma, and NEU-like cells were found predominantly in several IDH/H3-WT samples (Figures S9A and S9B). Then, examining the paired samples confirmed our earlier finding that non-neoplastic oligodendrocytes are enriched post-therapy but failed to observe any significant cell state shifts within the neoplastic cell compartment (Figures S9C and S9D).

Transcription factors jointly regulate pHGG neoplastic cell states

We then aimed to extend our characterization of these cell states via our single-nucleus chromatin accessibility data. After reintegrating and annotating the putative neoplastic population in our snATAC-seq data, we captured all the cell states defined transcriptionally in the snRNA-seq data, confirmed enrichment of chromatin accessibility in differentially expressed genes, and observed significant concordance with snRNA-seq across samples (Figures 3A, 3B, S10A–S10C, and S11A–S11F). As expected, we observed significant heterogeneity between patients and therapeutic time points and no significant shifts in neoplastic cell state post-therapy (Figure 3C).

We then aimed to identify the transcription factors that regulate each cell state, first by using chromVAR[38] to assess differential accessibility of transcription factor motifs (Table S7). Consistent with previous reports,[22,39] motifs for the AP1 family of transcription factors (e.g., FOS, JUN, and JDP2) were enriched in the mesenchymal state (Figure 3D). Notably, these motifs were also enriched in the Transition 2 state. Both the AC-like and GPC-like states were enriched for RFX factor motifs, and the OPC/NPC-like, OC-like, and NEU-like states were enriched for proneural transcription factors (e.g., ASCL1/2, NHLH1, and LHX4) (Figure 3D). To support the accuracy of our snATAC-seq cell state annotations, we performed single-nucleus multiomic (RNA+ATAC) sequencing on three samples and recovered similar motif enrichment, given the paired transcriptomic cell state annotations (Figure S10E).

Next, we constructed a transcriptional regulatory network (TRN) for each cell state by integrating our snRNA-seq and snATAC-seq data to predict state-specific enhancer-promoter interactions and transcription factor-target gene pairs (Table S8). These TRNs revealed substantial cooperativity between transcription factors in regulating cell-state-specific gene expression (Figures 3B, 3E–3G, and S11G–S11L). The RFX factors were predicted to regulate both the AC-like and GPC-like cell states.[30] SOX4 was predicted to regulate both the NEU-like and OPC/NPC-like states through cooperation with other transcription factors including LHX1 and KLF12, respectively (Figures 3E and 3F). The AP1 factors and RUNX1 were predicted to jointly regulate the MES-like state. RUNX1 was predicted to target the top differentially expressed genes in the MES-like state, and *RUNX1* expression itself was upregulated in MES-like neoplastic cells post-therapy (Figure 3F). While RUNX1 has been recognized as a contributor to mesenchymal GBM,[40] these results implicate the RUNX1 transcription factor as a central regulator of the MES-like transcriptional state. Moreover, it remained a central regulator when TRNs were constructed separately for the IDH/H3-WT and H3K27M subset (Figures S12 and S13). Overall, this analysis revealed the overlapping transcriptional regulatory interplay underlying the spectrum of neoplastic phenotypes.

(G) Cell-type proportions for each cell state projected onto a dataset of the developing fetal human brain.[13] tRG, truncated radial glia; uRG, unknown radial glia; IPC, inhibitory neuronal progenitor cell; RG, radial glia; EN, excitatory neuron; IN, interneuron; Astro, astrocyte; GPC; glial progenitor cell; OLC, oligo-lineage cells.
(H) Hypoxia signature score was computed as the mean value per cell state and per sample. Significance was assessed using the Kruskal-Wallis test.
(I) RNA velocity gradients of the neoplastic cells demonstrating hierarchical trajectories.
(J) Shifts in neoplastic cell state proportions for each patient between initial resection and post-therapy time points in snRNA-seq (n = 14 initial/post-therapy paired samples). Post-therapy samples were merged for one patient with three longitudinal samples. A two-sided Wilcoxon signed-rank test for paired samples was used.
(K) Heatmap of cell state shifts for each neoplastic cell state and patient, colored by the difference in percentage between the post-therapy and initial resection samples. Patients and cell states are clustered using hierarchical clustering.

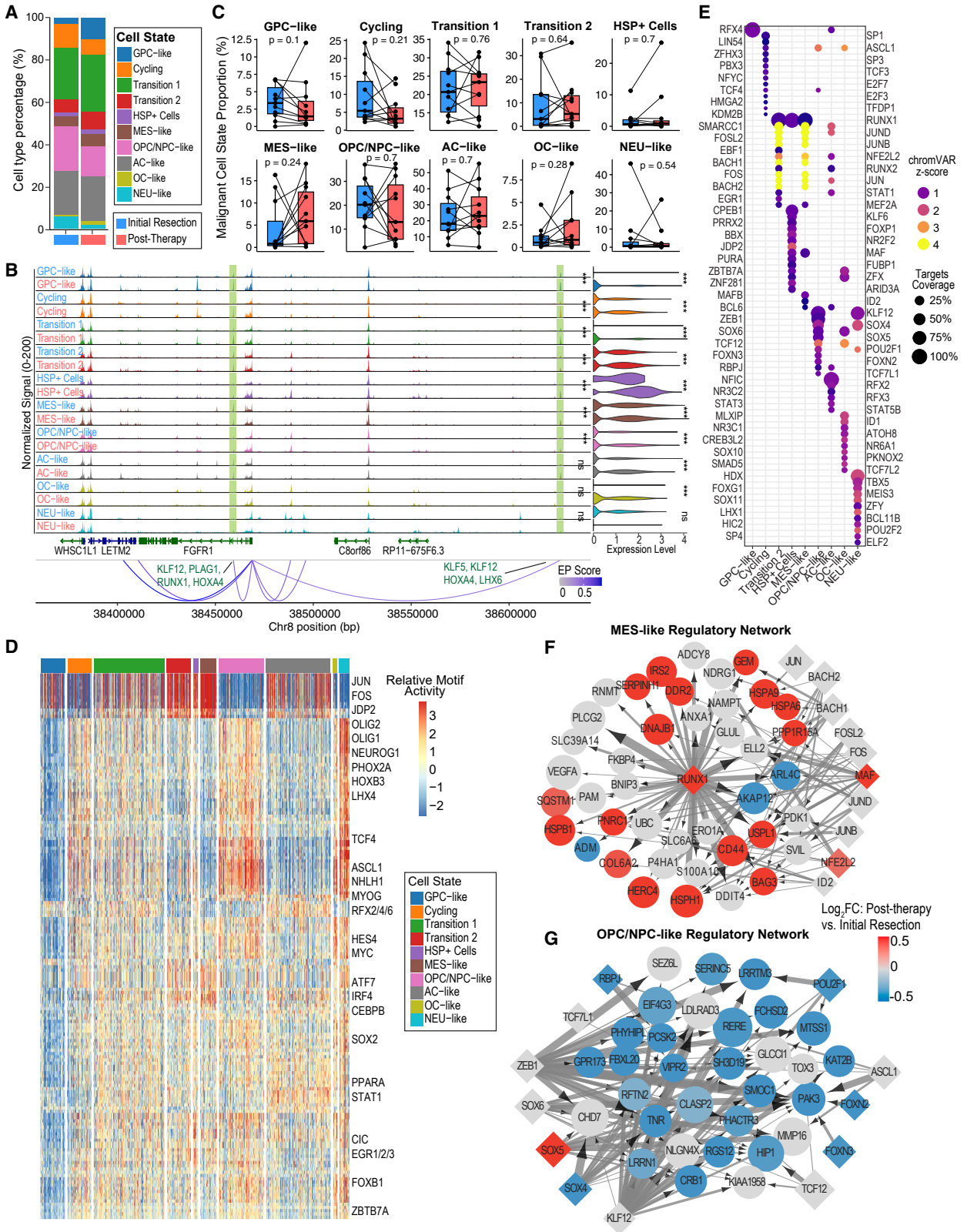

(legend on next page)

Tumor immune microenvironment is dominated by diverse myeloid populations

After defining the neoplastic cell states in pHGG, we sought to characterize the immune microenvironment. T cells comprised ~2% of the cells captured via snRNA-seq and were primarily found in two post-therapy specimens (Figures 1B–1D). One progressive H3G34R/V-mutant case was a notable outlier, with T cells representing ~22% of cells captured (Figure 1D). A low T cell abundance with outliers up to ~20% of total cell composition is consistent with adult GBM.[22] Myeloid cells comprised ~9% of the snRNA-seq data and were captured in each patient, so we selected this population for further analysis. After reintegration (Figures S14A–S1C), we identified 11 distinct myeloid populations that were manually annotated based on their differentially expressed genes and transcriptional regulons (Figures 4A–4C and S14D–S14H; Table S9). Most samples contained a distribution of myeloid subpopulations, while a few samples were dominated by a single subtype (Figure S14G). Additionally, these cells formed a continuous phenotypic spectrum, including resident microglia and bone-marrow-derived macrophage ontogenies (Figure S14D).

The myeloid subpopulations included tissue-resident microglia, dendritic cells, and multiple tumor-associated macrophage (TAM) subsets that have been previously characterized across multiple solid tumor types[24,25,42–44] including gliomas. This includes pro-angiogenic TAMs differentially expressing *VEGFA* and glycolytic enzymes (i.e., *HK2* and *ENO2*), lipid-associated TAMs (*PPARG* and *LPL*), inflammatory TAMs (*NFKB1* and *IL1B*), interferon (IFN)-responsive TAMs (*IFIT2*, *IFIT3*, and *ISG15*), as well as two additional populations of putative bone-marrow-derived macrophages (BMD): BMD TAM 1 (*F13A1*, *TMEM163*, and *MS4A4E*) and BMD TAM 2 (*TGFBI*, *MALT1*, and *RGS2*). Microglia were primarily stratified into pre-active microglia (*CCL3*, *EGR3*, and *NFKBID*) and homeostatic microglia (*P2RY12* and *TMEM119*) (Figures 4A–4C), reflecting a classification observed in both human and mouse.[45–47] Consistent with prior observations in adult glioblastoma, we found an overall shift in myeloid populations from microglia to bone-marrow-derived macrophages after therapy across the full cohort (Figures 4D and 4E).[22] On a sub-group analysis of IDH/H3-WT patients, we found that pre-active microglia decreased within the myeloid fraction in all IDH/H3-WT patients (Figure S14I). Given that myeloid population shifts were highly variable between patients, we applied a generalized linear mixed model approach (Table S10) to identify pathway-level changes in pseudobulk myeloid cells during tumor progression. We observed upregulation of interferon and inflammatory response pathways and downregulation of pathways related to proliferation and cellular metabolism (e.g., oxidative phosphorylation and E2F targets) (Figure 4F).

Previous studies have found that glioma-associated macrophages differentially interact with neoplastic cell states, altering their activity and differentiation status.[22,24,48] Indeed, we observed differential correlations in frequency between neoplastic cell states and myeloid subtypes across the 63 snRNA-seq datasets (including two regions for most samples). The MES-like state was associated with pro-angiogenic TAMs, while the OPC/NPC-like state was associated with homeostatic microglia (Figure 4G). Consequently, we aimed to elucidate how these pHGG-associated myeloid subpopulations interact with our newly defined pHGG-specific neoplastic cell states through an analysis of inferred ligand-receptor interactions (Figures 4H and S15; Table S11). We observed a broad set of bidirectional cellular interactions. Importantly, myeloid cells expressed genes that have the potential to mediate multiple neoplastic cell functions both through direct contact and secreted factors. These interactions included processes involved in regulating growth and proliferation (e.g., SPP1-CD44 and HBEGF-EGFR/ERBB2), cell adhesion and migration (e.g., FN1-ITGA3/ITGB1), and modulation of electrochemical or synaptic properties (e.g., CALM1-KCNQ5) (Figure S16). The AC-like and Transition 2 cell states were predicted to receive intercellular signals most broadly across myeloid subtypes with receptors including FGFR1, IGF1R, and CD44, which is specifically known to interact with a range of ligands (e.g., HBEGF, PSEN1, SPP1, and VEGFA) and has a critical role in adult glioma.[49–51] In contrast, the GPC-like and Transition 1 populations were the most inert neoplastic states (Figure 4H). These results were supported at the pathway level using CellChat[52] to aggregate individual interactions (Figure S17). Lastly, using spatial transcriptomics

Figure 3. Transcriptional regulation of pHGG neoplastic cell states

(A) Stacked bar plot of cell-type proportions of neoplastic cell states across dataset comparing initial resection and post-therapy samples. AC, astrocyte; GPC, glial progenitor cell; MES, mesenchymal; OC, oligodendrocyte; OPC, oligodendrocyte progenitor cell; NPC, neural progenitor cell; NEU, neural.

(B) Representative ATAC signal tracks of *FGFR1* locus and gene expression across cell states and time points. The link track represents the predicted enhancer-promoter interactions colored by the regression coefficient, and the TF motifs present at the enhancer peaks are indicated. Differentially accessible peaks between time points are highlighted. ***$p < 0.0001$, significance in gene expression or accessibility in *FGFR1*; ns, not significant, using one-sided Wilcoxon rank-sum test.

(C) Shifts in neoplastic cell state proportions for each patient between initial resection and post-therapy time points in snATAC-seq ($n = 11$ paired samples). Post-therapy samples were merged for one patient with three longitudinal samples. A two-sided Wilcoxon signed-rank test for paired samples was used.

(D) Heatmap of differential transcription factor (TF) motif accessibility in each pHGG neoplastic cell state. Values are *Z* score-normalized deviation scores calculated using chromVAR. The differential TF accessibility analysis was performed by a Wilcoxon rank-sum test, comparing chromVAR deviation score between each cell state and the other cell states. The top 20 differential TFs are displayed for each state.

(E) Overview of top 15 significant transcriptional regulators for each neoplastic cell state based on predicted enhancer-promoter interactions and TF-target gene pairs. The size of the dot indicates the fraction of the total gene targets in the network regulated by each TF. Color indicates chromVAR deviation *Z* score as in (D).

(F–G) Transcriptional regulatory networks (TRNs) for (F) MES-like state and (G) OPC/NPC-like state, showing top 50 upregulated genes and top 15 TFs in each TRN. TRNs represent all cells within the respective clusters across patients and time points. Diamond nodes represent TFs, and circle nodes represent target genes. Node size is proportional to the average gene expression for target genes and average chromVAR *Z* score for TFs. Node color is proportional to the average $\log_2$ fold change of the gene in that cell state post-therapy across all cells. Edge line thickness is proportional to the linear regression coefficient for the predicted enhancer-promoter interaction and the fraction of cells with chromatin accessibility at the enhancer peak.

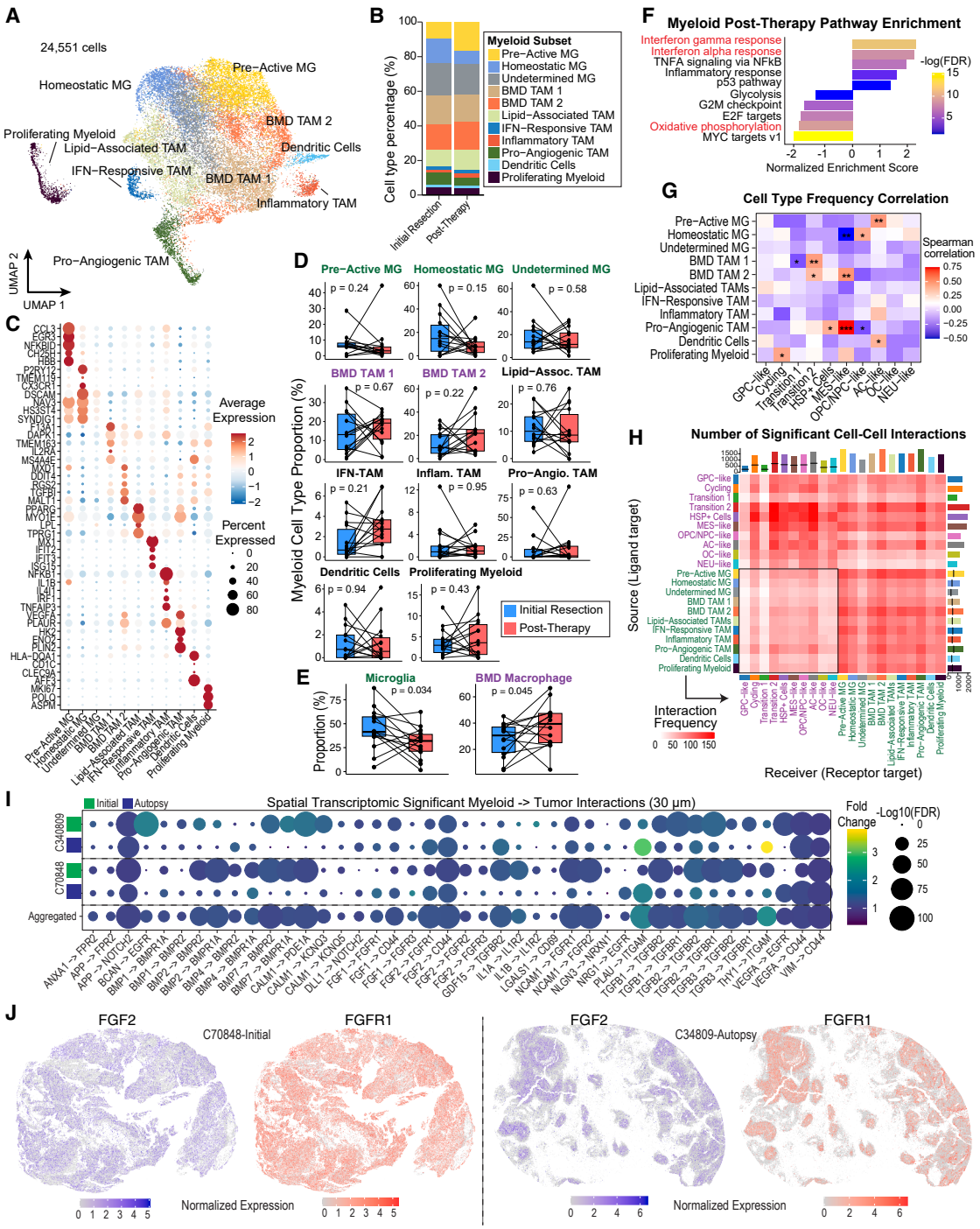

Figure 4. The myeloid response to progression and therapy

(A) UMAP projection of annotated tumor-associated myeloid cell populations identified in the integrated longitudinal pHGG snRNA-seq atlas (24,551 cells). BMD, bone-marrow-derived; MG, microglia, TAM, tumor-associated microphage.

(B) Stacked bar plot of myeloid cell-type composition across dataset comparing initial resection and post-therapy samples.

(C) Expression of representative genes across myeloid populations in snRNA-seq data.

(D) Shifts in myeloid cell-type proportions for each patient between initial resection and post-therapy time points in snRNA-seq (n = 14 initial/post-therapy paired samples). Post-therapy samples were merged for one patient with three longitudinal samples. A two-sided Wilcoxon signed-rank test for paired samples was used.

(E) Shifts in microglia cell-type proportions (pre-active, homeostatic, and undetermined) and bone-marrow-derived TAM proportions (BMD TAM 1 and BMD TAM 2) between initial resection and post-therapy time points in snRNA-seq as in (D). A one-sided Wilcoxon signed-rank test for paired samples was used.

(legend continued on next page)

(Table S12), we validated that myeloid-to-tumor ligand-receptor interactions were enriched among spatially proximal cells within several key pathways, including FGF, BMP, TGFβ, NOTCH, and CD44 signaling (Figures 4I and 4J). Taken together, this analysis provides a comprehensive characterization of pHGG myeloid subtypes and suggests that TAM populations differentially co-exist with neoplastic cell states.

Mapping the spatial landscape of pHGG

Complex topographic localization of neoplastic and immune populations in adult gliomas yields spatial niches with distinct molecular functions and therapeutic vulnerabilites.[53–58] To characterize the spatial landscape of pediatric HGG, we employed co-detection by indexing (CODEX) spatial proteomics with a 52-plex panel on 11 whole-slide formalin-fixed paraffin-embedded (FFPE) samples that had paired snRNA-seq data, including three IDH/H3-WT patient-matched longitudinal pairs (Figure 5A; Tables S13 and S14). After confirming appropriate antibody staining morphology and co-localization, we confirmed that our CODEX panel was able to resolve gross anatomical compartments including bulk tumor, gray matter, and white matter (Figures 5B and S18). Then, after segmenting single cells, computational integration, and clustering, we annotated over 7.5 million single cells (Figures 5C and S19). We captured the primary axis of neoplastic cell states from proneural (SOX2, OLIG1, and OLIG2) to astrocytic/mesenchymal (CD44, VIM, and GFAP). We also observed a tumor cell population with high expression of APOE and SPP1 that was predominantly identified in peri-necrotic regions (Figure S20A). Neoplastic cell states were distributed heterogeneously both between and within samples, with regions of the tumor predominated by patches of either proneural or mesenchymal tumor cells (Figures 5D and 5E).

The myeloid populations formed a phenotypic distribution including microglia and macrophages (Figures 5E and S19A). We identified a macrophage population that strongly co-expressed CD163 and CD206, a second macrophage population characterized by high HLA-DR expression, and a large population of MPO^+ myeloid cells with heterogeneous morphologies, likely representing both neutrophils and MPO^+ mononuclear cells as previously reported[20] (Figures S19C and S19D). This MPO^+ population had a high expression of HIF-1α and was primarily found as large infiltrates in peri-necrotic regions in several samples (Figures S19E and S20B). While we identified small populations of $CD4^+$ and $CD8^+$ T cells, inspection of the images revealed that T cells were predominantly located within vessels or concentrated in areas of hemorrhage (Figure S20C). This demonstrates that blood contaminants in tissue may confound analysis of single-cell sequencing of rare immune populations. Lastly, we observed spatially restricted expression of immune checkpoint molecules including CD47 and programmed death-ligand 1 (PD-L1) (Figure S20D).

Oligodendrocytes coordinate post-therapy-enriched cellular neighborhoods

To systematically identify recurrent spatial patterns across all samples, we first performed unsupervised neighborhood analysis and identified 15 cellular neighborhoods (CNs) that we manually annotated based on their relative enrichment of cell types (Figure 5F). These neighborhoods were heterogeneously distributed across samples and captured expected anatomic compartments including gray matter (CN2, mature neurons), white matter (CN6, mature oligodendrocytes), and infiltrating tumor regions (CN7, oligodendrocytes and tumor cells) (Figures 5G and S21). Additionally, this analysis highlighted localized regions predominated by different tumor cell states (i.e., proneural, intermediate, and mesenchymal neighborhoods), as well as MPO^+ infiltrates, and a vascular neighborhood (Figure 5F). Tumor cells tended to co-localize with cells sharing the same phenotype, such as proneural tumor cells localizing with other proneural tumor cells (Figures 5D and F). Notably, the mesenchymal tumor cell type was not co-enriched with proneural tumor cells in any neighborhood either overall or when the neighborhoods were computed separately by subtype (Figures 5F and S22). Immune cells were differentially localized across cellular neighborhoods. Microglia were enriched in areas of normal brain, primarily gray matter (Figure 5F) and were observed to be concentrated at the tumor-normal boundary (Figure S20E). Macrophages and T cells were jointly enriched in an immune-enriched neighborhood (CN1), a perivascular neighborhood (CN5), a vascular tumor neighborhood (CN11), a mesenchymal tumor neighborhood (CN3), and a tumor/immune neighborhood (CN9). Immune cells were relatively depleted in all neighborhoods that had a significant enrichment of proneural tumor cells (Figure 5F). By examining distances from tumor cells to myeloid cells, we found that proneural and mesenchymal tumor cells were most consistently enriched near HLA-hi macrophages, while peri-necrotic tumor cells co-localized with MPO^+ myeloid cells and unclassified macrophages. Moreover, we found that mesenchymal tumor

(F) Gene set enrichment analysis (GSEA) of Hallmark pathways within myeloid cells. A linear mixed model was used to identify differentially expressed genes between time points while accounting for individual patient variability.

(G) Heatmap of Spearman correlation coefficients between neoplastic cell state proportions and myeloid proportions across snRNA-seq dataset. Each region within a single sample was considered separately for this analysis, yielding $n = 63$ data points (two regions profiled for most tumor specimens). The frequency of each neoplastic cell state (out of all malignant cells) and the fraction of each myeloid state (out of all myeloid cells) were correlated for each data point. p values were adjusted using the Benjamini-Hochberg method; $^{***}p < 0.001$, $^{**}p < 0.01$, $^{*}p < 0.05$.

(H) Heatmap showing number of significant interactions between myeloid and neoplastic cell populations across dataset. Interactions were inferred using LIANA[41] and filtered for aggregated consensus rank (adjusted p value < 0.05). Bars above the heatmap represent total number of significant interactions received (down columns), and bars to the right of the heatmap represent total number of significant interactions sent (across rows) for each cell type, with black lines indicating subset of interactions between myeloid and neoplastic cells. Box highlights interactions from myeloid cells to neoplastic cells.

(I) Significant myeloid-to-tumor cell-cell interactions in Xenium spatial transcriptomics data. Dot color indicates fold change of observed ligand-receptor score over null distribution, and dot size indicates the FDR, with a pseudocount of 1e−100. Ligand-receptor pairs that are significant (FDR<0.05) in at least two samples and upon aggregation are shown.

(J) Two representative Xenium samples indicating spatial co-localization of *FGF2* and *FGFR1*.

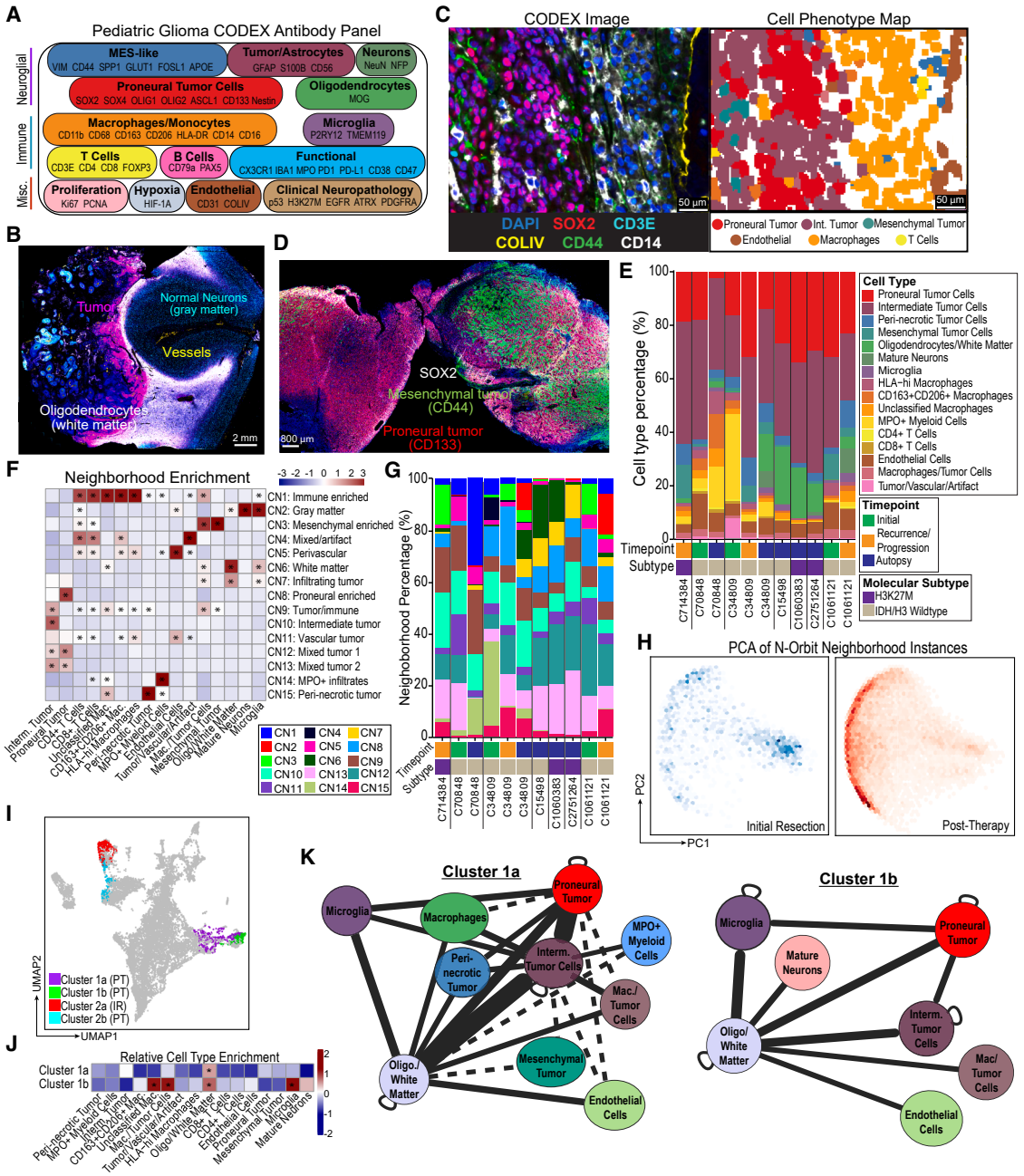

Figure 5. CODEX imaging reveals microenvironmental changes in pHGG during therapy

(A) Diagram showing the 51-antibody CODEX panel split by target cell population or cellular function.

(B) Representative CODEX image highlighting tumor mass and substructures of the normal brain. DAPI (blue), Collagen IV (yellow), Neu (cyan), SOX2 (magenta), MOG (white). Scale bars: 2 mm.

(C) CODEX image with selected fluorescent markers (left) paired with cell phenotype map (right). Segmentation masks of individual cells are colored by their identity. Scale bars: 50 µm.

(D) Representative CODEX image demonstrating spatially restricted tumor cell state populations. Proneural tumor cells are stained by CD133 (red) and SOX2 (white) and mesenchymal tumor cells stained by CD44 (green). Scale bars: 800 µm.

(E) Cell-type proportions in each CODEX sample.

(F) Heatmap showing relative enrichment of the cell types present in neighborhoods, normalized across neighborhoods (by column). Significant positive cell-type enrichments in each neighborhood were calculated using a hypergeometric test, adjusted using the Benjamini-Hochberg method. * adjusted $p < 0.001$.

(G) Neighborhood proportions in each CODEX sample.

(H) Principal-component analysis density plots of the N-Orbit-derived neighborhood distance matrix, split by time point.

(legend continued on next page)

cells were closest to endothelial cells, while peri-necrotic tumor cells were furthest from vasculature (Figure S23).

Next, we sought to identify spatial patterns that were enriched post-therapy. To mitigate the significant heterogeneity between samples, we identified neighborhoods on each sample individually and utilized our recently developed N-Orbit framework[59] to project each contiguous neighborhood instance using principal-component analysis. We found that the first principal component (PC1) captured the time point effect (Figures 5H, S24A, and S2B). Then, we identified two clusters that were among the top contributors to PC1 and had subclusters that were enriched in the initial resection or post-therapy time points (Figures 5I, 5J, S24C, and S24D). Each cluster had representation from all patients with samples in those time points. Tracing the neighborhood instances in the post-therapy cluster 1 back to their enriched N-Orbits revealed an enrichment for oligodendrocytes that primarily interacted with proneural and intermediate tumor cells with secondary interactions involving immune cells such as microglia (Figures 5K and 5L). Cluster 2 primarily captured vascular features (Figures S24E–S24G). These results suggest that spatial coordination with oligodendrocytes is enhanced post-therapy and that these interactions favor proneural and intermediate over mesenchymal tumor cell phenotypes.

Tumor subclone dynamics reveal recurrent genomic alterations

We next aimed to apply our longitudinal data to identify genomic and transcriptional shifts during progression and therapy. We first utilized large-scale CNVs to trace tumor subclones across patient-matched samples with Clonalscope,[60] which integrates snRNA-seq and matched whole-genome sequencing (WGS) data. Neoplastic subclones were defined at the earliest time point for each patient and traced to the later therapeutic time points to assess populations that have expanded or regressed. Through this approach we identified lineage-traced neoplastic subclones on 14 patients, ranging from four to nine subclones per patient, with variable clonal dynamics across time points (Figure 6A). We identified recurrent CNVs including copy-number gains on chromosomes 1q, 7p/7q, 8q, 19p/19q, and 20p and copy-number losses on chromosomes 5p/5q, 6q, 10p/10q, and 14q (Figures 6B and 6C). Clustering of gene-level CNVs across tumor subclones revealed recurrent modules of highly correlated CNVs across patients, indicating that similar patterns of chromosome alterations dynamics occur during disease progression (Figure 6D). Notably, some alterations occurred more frequently on expanded subclones (e.g., gain on chr18p and chr19q and loss on chr14q), suggesting that these alterations may confer a survival advantage (Figure 6E; Table S15). However, we found that larger genomic/subclonal shifts were not correlated with larger shifts in neoplastic cell state composition (Figure 6F). Lastly, we compared the expanded subclones to the remaining malignant cells for each patient using a gene set enrichment analysis. This revealed an upregulation of immune-related pathways in the majority of patients, suggesting that the selection of neoplastic phenotypes may be connected to the tumor microenvironment (Figure 6G; Table S16).

Longitudinal analysis uncovers tumor-cell-intrinsic targets

We then applied an analogous generalized linear mixed model (GLMM) approach to identify genes and pathways that were upregulated across therapeutic time points over all neoplastic cells, accounting for individual patient variability. Despite not observing population-level cell state shifts in the neoplastic compartment, this analysis yielded 627 significantly upregulated genes and 1,551 significantly downregulated genes (adjusted $p < 0.05$) (Table S17; Figure 7A). Examining pathway-level changes revealed an upregulation of type I and type II interferon response pathways and the neuroactive ligand-receptor interactions gene set as well as downregulation of pathways related to cell proliferation and metabolism, primarily oxidative phosphorylation (Figures 7B and S25A). We hypothesized that the effect of radiation may be causally associated with the observed transcriptional changes. Indeed, we uncovered many of the same pathway changes in treatment-naive pHGG cell lines treated with ionizing radiation using an analogous GLMM approach to analyze bulk RNA-seq data on three cell lines before and after treatment (Figures 7C, 7D, S25B, and S25C). This implicates the direct effects of radiotherapy in the suppression of cell cycling and oxidative phosphorylation and the increase in interferon and neuroactive signaling.

We then aimed to utilize this neoplastic-cell-specific longitudinal analysis to identify tumor-cell-intrinsic drug targets in pHGG cell lines. To prioritize gene targets, we screened genes that were differentially upregulated during progression against multiple drug target databases and the Cancer Dependency Map (DepMap), as well as considered their roles as receptors in the tumor microenvironment (Figures 7E, S25C, and S25D; Tables S18 and S19). After curating targets to validate, we screened 24 pharmacological compounds across six pHGG cell lines to assess their impact on cell proliferation and viability over a 72-h time course (Table S20). Deconvolution of bulk RNA-seq data on these cell lines demonstrated that they recapitulate the spectrum of neoplastic cell states observed in patient samples (Figure S25E). We verified a cytotoxic effect of AZD4547 (FGFR inhibitor), danusertib (aurora kinase/ABL kinase/FGFR1 inhibitor), panobinostat (non-selective HDAC inhibitor), and trametinib (MEK inhibitor) across cell lines (Figures 7F, S25D, S26, S27A, and S28). Multiple genes related to apoptosis and inflammasome activation were upregulated after progression on treatment including caspases (*CASP1*, *CASP4*), *BCL2L1*, and *BCL6.* Indeed, inhibition of CASP1 with belnacasan and

(I) Clusters of neighborhoods that were top contributors to PC1, represented on the UMAP projection. IR indicates significant enrichment in initial resection samples; PT indicates significant enrichment in post-therapy samples.

(J) Cell-type enrichment of clusters 1a and 1b. Colors represent log odds ratio. *$p < 0.05$ by hypergeometric test.

(K) Summary subgraphs of post-therapy enriched neighborhood instance clusters 1a and 1b, derived from their enriched N-Orbits. Solid lines indicate 1-orbit relationships, with edge weights indicating relative frequency of cell-type interactions among enriched N-Orbits. Dashed lines indicate two-orbit relationships. Self-edges indicate monotypic interactions of that cell type.

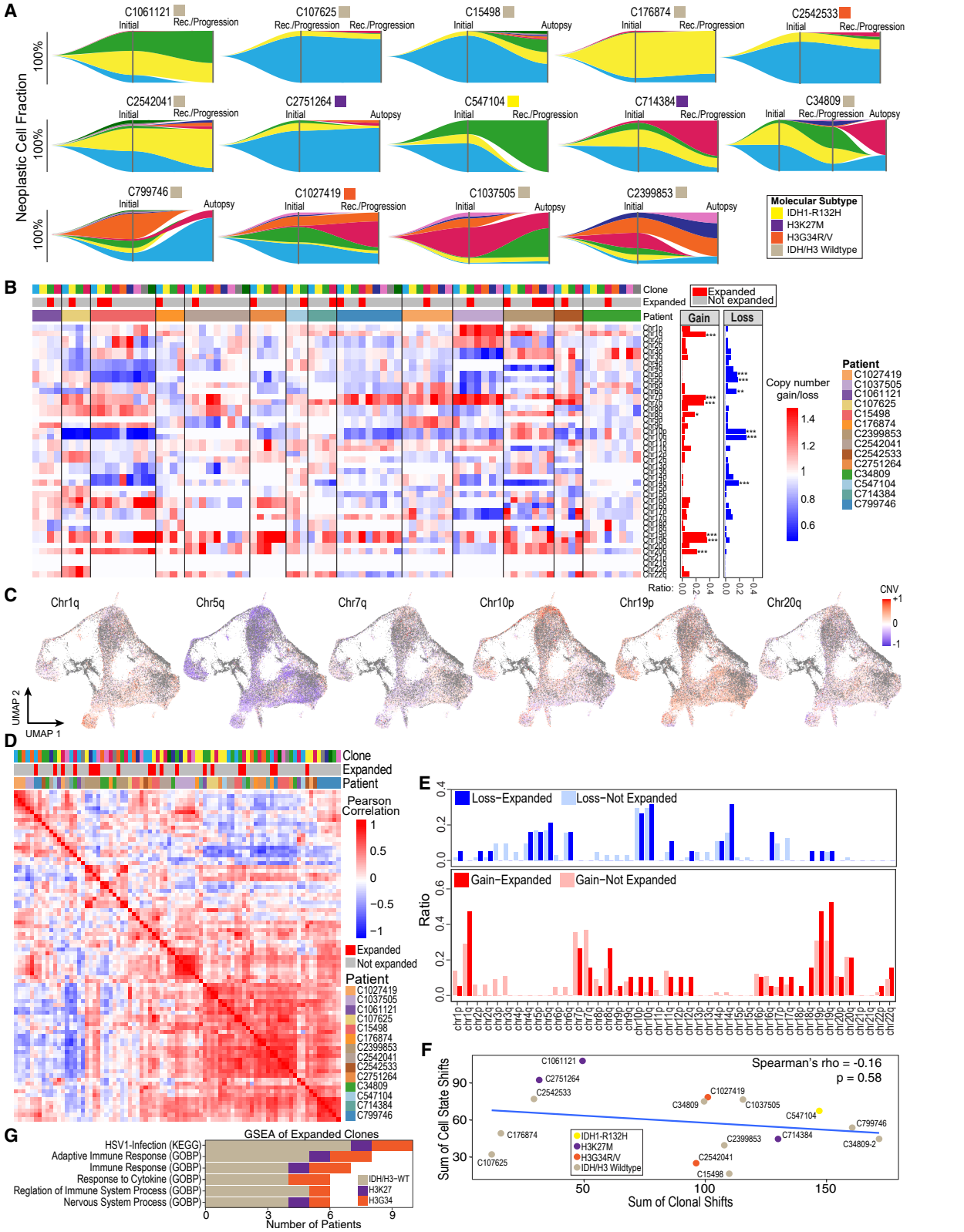

(legend on next page)

inhibition of BCL-2 with navitoclax or venetoclax reduced proliferation *in vitro* compared to DMSO controls (Figures S26 and S27A). Notably, trametinib synergized with navitoclax across multiple cell lines, providing evidence that apoptosis inhibitors could improve response to existing therapies (Figure 7G). Consistent with our pathway analysis, we observed significant upregulation of multiple genes involved in electrochemical and synaptic communication, which has been shown to support glioma progression and invasion.[61–63] The selective CHRM3 antagonist, J-104129, resulted in significant cell death through the induction of apoptosis (Figures 7D, S25F, S26, and S27A). The selective $GABA_A$ receptor antagonist, gabazine, had a mild antiproliferative effect across cell lines (Figures S20 and S27A). Lastly, our screening highlighted secretory phospholipase A2 (sPLA2) for further exploration in pediatric glioma, with a dose-dependent response upon treatment with the PLA2-inhibitor varespladib in all six cell lines and was found to act through the induction of apoptosis (Figures 7D, S25F, and S27B).

DISCUSSION

In this study, we profiled the single-cell transcriptional, chromatin accessibility, and spatial landscape of pediatric high-grade glioma (pHGG) longitudinally under therapeutic pressure and disease progression. We defined a set of cross-subtype pediatric HGG neoplastic cell states that reflect conserved hierarchical differentiation dynamics. This adds to the growing literature that supports overlapping patterns of derangements in neurodevelopmental differentiation across multiple CNS tumors, including IDH-mutant glioma,[33] H3K27M glioma,[19] adult glioblastoma,[11] and ependymomas,[30] although the nomenclature and framework for understanding these phenotypes and their relationship to the cells of origin continues to evolve. We found that T cells and mural cells were overall very scarce but highly enriched within a small number of samples, consistent with observations in adult glioma.[27] We did not observe a consistent pattern of neoplastic cell state shifts, but we did observe a shift from microglial to macrophage phenotypes within the myeloid compartment, which is also consistent with adult GBM.[22] Of note, systemic glucocorticoids, given to many neurosurgical patients, may bias immunological changes in the microenvironment. We identified an increase in non-neoplastic oligodendrocytes and found that oligodendrocytes coordinate spatial motifs that are enriched post-therapy. This could reflect oligodendrocyte recruitment and proliferation or could be explained by increased tumor invasion and integration into the surrounding brain parenchyma. Further *in vitro* and *in vivo* studies are needed to clarify this process, isolate the impact of tumor progression versus therapeutic pressures, and identify clinically actionable mechanisms. There is also a need for subsequent investigation of the remaining non-malignant neuronal and astrocytic populations, which clustered closely with the neoplastic cells.

Synaptic electrochemical signaling through multiple receptors has been increasingly implicated in adult and pediatric glioma progression,[62] including acetylcholine,[63–66] dopamine,[67–69] and GABA.[70–72] We found that neuroactive signaling and interferon response pathways were broadly upregulated in pHGG, and *in vitro* experimentation indicated that ionizing radiation may directly upregulate these pathways. Interferon signaling has been implicated in a wide range of injury-response mechanisms, therefore such activation in pHGG may partly reflect generic neuroinflammatory programs or therapy-induced effects rather than purely tumor-intrinsic biology. Through *in vitro* drug screening, we identified a dependency on the M3 muscarinic receptor and also nominated sPLA2 for further pre-clinical study. Phospholipases are enzymes that hydrolyze phospholipids into precursor fatty acids, which have roles in cell signaling, metabolism, and inflammation. Phospholipase A2 has been implicated in multiple cancer types including colorectal cancer,[73] skin cancer,[74] and adult glioblastoma,[75,76] in which it has been shown to inhibit apoptosis and activate EGFR signaling.[77]

Overall, our study sheds light onto the molecular mechanisms of pHGG and provides an extensive, high-quality, and scalable multiomic atlas. This dataset can be used for the rapid annotation and comparison of additional samples as well as to interrogate a broad spectrum of hypotheses related to the transcriptional, epigenetic, mutational, microenvironmental, and spatial features of this incurable disease.

Limitations of the study

The findings in this dataset must be contextualized with the significant heterogeneity intrinsic to the patient cohort. The small

Figure 6. Tumor subclone dynamics across patients

(A) Fishtail plots showing shifts in tumor subclone populations across longitudinal time points for 14 patients. Colors represent individual subclones.

(B) Left, heatmap of average CNVs within each tumor subclone at the chromosome arm level across 14 patients using Clonalscope. Clone color (top row) corresponds to the patient-specific subclone shown in (A). Right, ratio of binarized copy-number gain or loss for each chromosome arm, defined as having an average CNV >1.25 or average CNV <0.75, respectively. For each chromosome arm, a Fisher's exact test was used to assess for recurrent copy-number alterations, adjusted using the Benjamini-Hochberg method. $^{***}p < 0.001$; $^{**}p < 0.01$, $^{*}p < 0.05$.

(C) UMAP projection of neoplastic cells colored by amplification or deletion of specific chromosome arm segments predicted by Clonalscope. Gray indicates insufficient sequencing coverage for Clonalscope CNV prediction of that particular chromosome arm segment.

(D) Correlation heatmap of subclones based on estimated copy-number variation (CNV) at the gene level. The CNV states of chromosome segments in each subclone were used to infer gene-level CNVs for comparison across the cohort.

(E) Ratio of binarized copy-number alteration (gain or loss) at the chromosome arm level comparing expanded and non-expanded clones. The ratio represents the number of subclones with copy-number gain or loss among all 84 subclones identified across patients. Expanded subclones were defined if they increased in proportion across time points and comprise at least 10% of the tumor population at the latest time point.

(F) Association between subclonal and cell state shifts, calculated as the sum of the differences in percentage composition across all subclones (*x* axis) or cell states (*y* axis) between each pair of consecutive time points ($n = 15$).

(G) Number of patients in which selected pathways are enriched in the expanded subclones (adjusted $p < 0.05$), colored by subtype of patient. GOBP, Gene Ontology Biological Process.

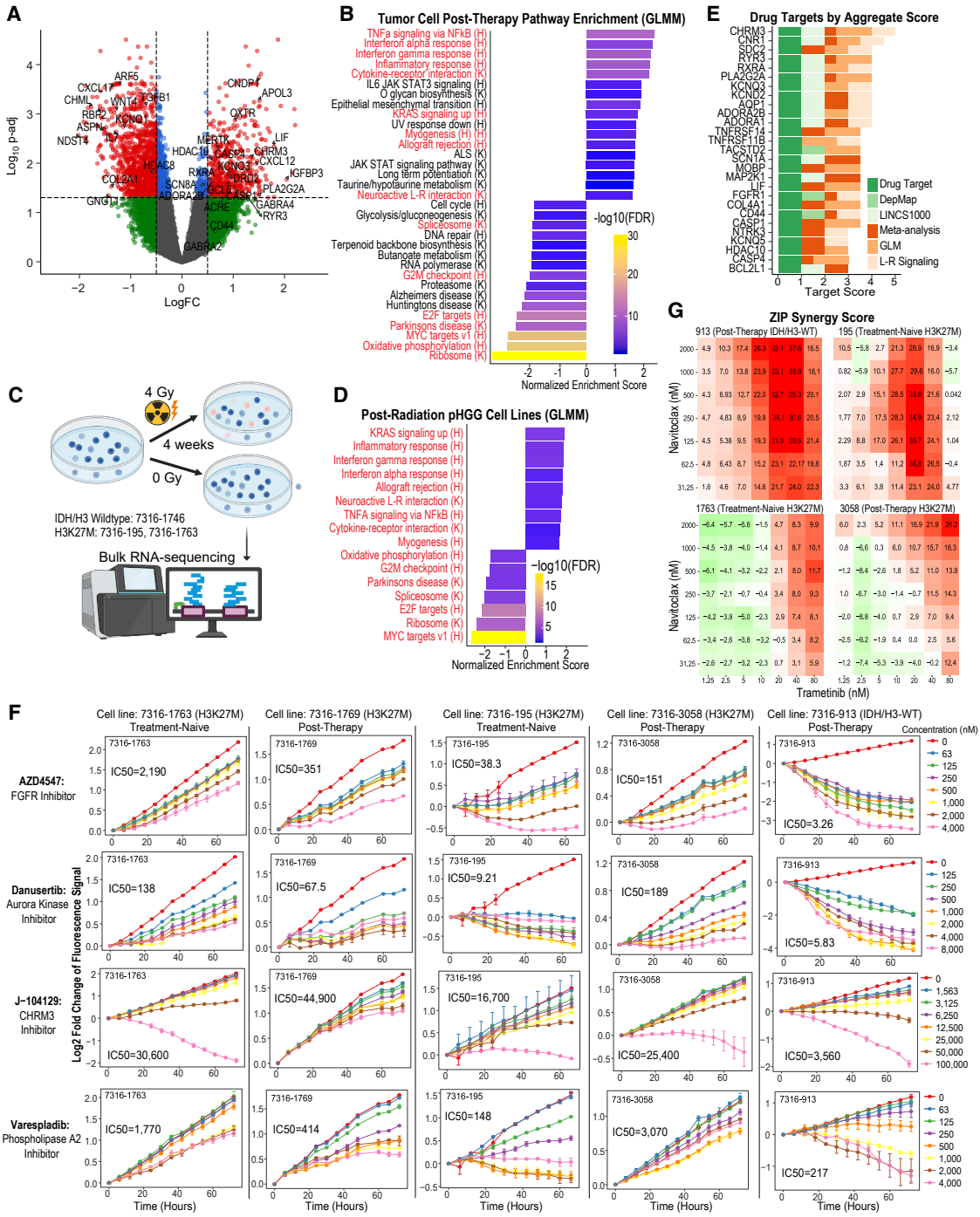

Figure 7. Identifying therapeutic sensitivities through *in vitro* drug screening

(A) A linear mixed model was used to identify differentially expressed genes within neoplastic cells overall between initial resection and post-therapy time points accounting for individual patient variability. Volcano plot shows the log fold change and adjusted *p* value for each gene included in the model, with selected genes labeled. Log fold change >0.5 and adjusted *p* value < 0.05 are indicated with dashed lines.

(B) Gene set enrichment analysis (GSEA) of Hallmark (H) and KEGG (K) pathways across all genes in (A) ranked by log fold change.

(C) Schematic of radiation experiment. Cells were treated with 4 Gy of ionizing radiation and allowed to recover for 4 weeks before undergoing bulk RNA sequencing.

(D) GSEA of post-radiation changes using analogous GLMM as in (B) using three pHGG cell lines. Significant pathways shared with (B) are shown and highlighted in red in both panels.

(legend continued on next page)

size and frequent inoperability of pHGG tumors significantly limit the number of high-quality samples that can be collected for multiomic profiling and necessitate the inclusion of postmortem samples from research autopsies. Specifically, diffuse midline gliomas were limited to thalamic tumors and did not include the more common pontine gliomas, which are typically not surgically resected. Moreover, the clinical course of pHGG is variable, and the treatment plans are individualized to each patient, including different combinations of chemo/immunotherapy and duration of radiotherapy. Additionally, the longitudinal samples were obtained after varying amounts of time at recurrence or autopsy, rather than after definitive treatment. Importantly, there are multiple tumor-intrinsic features of disease progression and tumor-extrinsic factors such as radiation or immunotherapy that can alter the microenvironment. Therefore, it is challenging to precisely disentangle the combined effects of molecular characteristics and treatment modalities on longitudinal cell state changes. We postulate that these factors jointly contribute to the plasticity between neoplastic cell states and range of cell state shifts observed between patients. Relatedly, the nomenclature and framework surrounding glioma cell states continues to evolve. While trajectory analyses describe a conserved topological structure, individual tumors do not uniformly complete a canonical trilineage hierarchy, suggesting that specific genetic drivers likely constrain these trajectories. Further studies are expected to elucidate the interplay between genetic, microenvironmental, and treatment-dependent mechanisms of resistance in pHGG. This could include integrating these data with the growing body of published, subtype-specific pediatric glioma datasets and larger retrospective cohorts of archived clinical specimens to fully substantiate these single-cell dynamics. Finally, our methods for prioritizing potential drug targets do not establish a predictive therapeutic model. Subsequent large-scale screening and *in vivo* validation are required to systematically identify pharmacologic targets and confirm clinical actionability.

RESOURCE AVAILABILITY

Lead contact

Requests for further information, reagents, and resources should be directed to and will be fulfilled by the lead contact, Kai Tan (tank1@chop.edu).

Materials availability

All materials used in this study are commercially available, as specified in the key resources table.

Data and code availability

- All primary sequencing and spatial data generated for this study are available through dbGaP under accession number phs002371 as part of the Human Tumor Atlas Network consortium (https://humantumoratlas.org/publications/hta4_2026_cell-reports-medicine_jonathan-h-sussman). This includes count matrices, multi-channel images, segmentation masks, and processed Seurat objects. The snRNA-seq data objects can be explored interactively on CELLxGENE at https://cellxgene.cziscience.com/collections/9ceda3d2-a55e-4b82-a91a-0190d947459a. The linkage between HTAN patient IDs and sample IDs is provided in Table S2. Bulk RNA-seq data from the *in vitro* experiments are deposited at NCBI GEO (accession GSE292623).
- Software and source code created for this study are publicly available on GitHub at https://github.com/tanlabcode/pHGG_Atlas.
- Any additional information required to reanalyze the data reported in this work is available from the lead contact (Kai Tan, tank1@chop.edu) upon request.

ACKNOWLEDGMENTS

The authors acknowledge the Children's Brain Tumor Network for collecting tissue and curating clinical information used in this study and the Children's Hospital of Philadelphia Pathology Core, Flow Cytometry Core, High-Throughput Sequencing Core, and Research Information Services for providing technical support. We are grateful to all the patients and their families who volunteered to participate in this study. This work was supported by the National Cancer Institute (NCI) Human Tumor Atlas Network grant under award #U2C CA233285 (K.T.). Additional support includes National Institutes of Health (NIH) grants U54HL165442 (K.T.), NIH grant F30-CA-268782 (J.X.), NIH Medical Scientist Training Program T32 GM07170, NIH grant F30-CA-277965 (S.B.), NIH grant F30-CA-298606 (B.X.), National Heart, Lung, and Blood Institute R38 HL143613 (D.A.O.), and NCI T32 CA009140 (D.A.O.). Additional funding was provided by the Parker Institute for Cancer Immunotherapy and V Foundation for Cancer Research, co-sponsoring a Parker Bridge Fellow Award (D.A.O.).

AUTHOR CONTRIBUTIONS

J.H.S., D.A.O., W.Y., N.M.A., T.D.R., K.C., and K.T. conceived and designed the study. S.McG., M.S., M.P.K., P.B.S., and K.C. provided patient samples. J.H.S., D.A.O., W.Y., J.R., A.P.-R., A.Y., B.X., J.S.T., J.X., S. Bandyopadhyay, Y.S., D.W.W., performed computational and statistical analyses. J.H.S., C.-H.C, A.M.Z., A.T., S. Brosius, I.S., K.J.A., U.Y.B., T.D.R. performed experiments. J.H.S., D.A.O., W.Y., J.R., J.X., S. Bandyopadhyay, O.E., A.E.B., R.S.V., N.M.A. performed data interpretation and biological analysis. N.Z., T.D.R., A.N.V., K.C., and K.T. provided funding and supervised the study. J.H.S, D.A.O., W.Y., and K.T. wrote the manuscript with input from all authors.

DECLARATION OF INTERESTS

The authors declare no competing interests.

STAR★METHODS

Detailed methods are provided in the online version of this paper and include the following:

- KEY RESOURCES TABLE
- EXPERIMENTAL MODEL AND STUDY PARTICIPANT DETAILS

(E) Top gene targets by aggregate ranking score. Criteria include screening against drug databases, LINCS1000 compound perturbations, DepMap, differential gene expression, and participation in ligand-receptor signaling as a receptor target.
(F) Selected growth curves from *in vitro* drug screening in human pHGG cell lines grown in spheroid culture. Cells were treated with drugs at indicated concentrations, and growth was monitored using a fluorescent reporter over 72 h of drug treatment (n = 24 control, 2 drug-treated replicates each). y axis indicates the log2 fold change of total fluorescence signal from the zero time point. Positive values indicate a net proliferation, while negative values indicate net cell death. IC_{50} values (in nM) are indicated for each drug and cell line. Data are shown as mean ± SEM with n = 2 replicates per condition.
(G) Synergy scores (zero interaction potency) for combinations of trametinib and navitoclax across concentrations. Median ZIP scores are 18.1 (913 cell line), 10.5 (195 cell line), −1.49 (1763 cell line), and 0.82 (3058 cell line).

SUPPLEMENTAL INFORMATION

Supplemental information can be found online at https://doi.org/10.1016/j.xcrm.2026.102766.

Received: July 31, 2025
Revised: February 2, 2026
Accepted: March 25, 2026
Published: April 23, 2026

REFERENCES

1. Ostrom, Q.T., de Blank, P.M., Kruchko, C., Petersen, C.M., Liao, P., Finlay, J.L., Stearns, D.S., Wolff, J.E., Wolinsky, Y., Letterio, J.J., and Barnholtz-Sloan, J.S. (2015). Alex's Lemonade Stand Foundation Infant and Childhood Primary Brain and Central Nervous System Tumors Diagnosed in the United States in 2007–2011. Neuro Oncol. *16*, x1–x36. https://doi.org/10.1093/neuonc/nou327.
2. Mackay, A., Burford, A., Carvalho, D., Izquierdo, E., Fazal-Salom, J., Taylor, K.R., Bjerke, L., Clarke, M., Vinci, M., Nandhabalan, M., et al. (2017). Integrated Molecular Meta-Analysis of 1,000 Pediatric High-Grade and Diffuse Intrinsic Pontine Glioma. Cancer Cell *32*, 520–537.e5. https://doi.org/10.1016/j.ccell.2017.08.017.
3. He, X., Zhao, W., Huang, J., Xu, J., Niu, S., Zhang, Q., Zhang, N., Jin, H., and Shen, G. (2022). Characteristics and trends of globally registered glioma clinical trials in the past 16 years. Ther. Adv. Neurol. Disord. *15*, 17562864221114355. https://doi.org/10.1177/17562864221114355.
4. Hatoum, R., Chen, J.-S., Lavergne, P., Shlobin, N.A., Wang, A., Elkaim, L.M., Dodin, P., Couturier, C.P., Ibrahim, G.M., Fallah, A., et al. (2022). Extent of Tumor Resection and Survival in Pediatric Patients With High-Grade Gliomas: A Systematic Review and Meta-analysis. JAMA Netw. Open *5*, e2226551. https://doi.org/10.1001/jamanetworkopen.2022.26551.
5. Louis, D.N., Perry, A., Wesseling, P., Brat, D.J., Cree, I.A., Figarella-Branger, D., Hawkins, C., Ng, H.K., Pfister, S.M., Reifenberger, G., et al. (2021). The 2021 WHO Classification of Tumors of the Central Nervous System: a summary. Neuro Oncol. *23*, 1231–1251. https://doi.org/10.1093/neuonc/noab106.
6. Wu, G., Diaz, A.K., Paugh, B.S., Rankin, S.L., Ju, B., Li, Y., Zhu, X., Qu, C., Chen, X., Zhang, J., et al. (2014). The genomic landscape of diffuse intrinsic pontine glioma and pediatric non-brainstem high-grade glioma. Nat. Genet. *46*, 444–450. https://doi.org/10.1038/ng.2938.
7. Jones, C., Karajannis, M.A., Jones, D.T.W., Kieran, M.W., Monje, M., Baker, S.J., Becher, O.J., Cho, Y.-J., Gupta, N., Hawkins, C., et al. (2017). Pediatric high-grade glioma: biologically and clinically in need of new thinking. Neuro Oncol. *19*, 153–161. https://doi.org/10.1093/neuonc/now101.
8. Bax, D.A., Mackay, A., Little, S.E., Carvalho, D., Viana-Pereira, M., Tamber, N., Grigoriadis, A.E., Ashworth, A., Reis, R.M., Ellison, D.W., et al. (2010). A Distinct Spectrum of Copy Number Aberrations in Pediatric High-Grade Gliomas. Clin. Cancer Res. *16*, 3368–3377. https://doi.org/10.1158/1078-0432.CCR-10-0438.
9. Wang, J., Huang, T.Y.-T., Hou, Y., Bartom, E., Lu, X., Shilatifard, A., Yue, F., and Saratsis, A. (2021). Epigenomic landscape and 3D genome structure in pediatric high-grade glioma. Sci. Adv. *7*, eabg4126. https://doi.org/10.1126/sciadv.abg4126.
10. WHO Classification of Tumours Editorial Board (2021). Central Nervous System Tumours, 5th ed. (Lyon: International Agency for Research on Cancer).
11. Neftel, C., Laffy, J., Filbin, M.G., Hara, T., Shore, M.E., Rahme, G.J., Richman, A.R., Silverbush, D., Shaw, M.L., Hebert, C.M., et al. (2019). An Integrative Model of Cellular States, Plasticity, and Genetics for Glioblastoma. Cell *178*, 835–849.e21. https://doi.org/10.1016/j.cell.2019.06.024.
12. Gojo, J., Englinger, B., Jiang, L., Hübner, J.M., Shaw, M.L., Hack, O.A., Madlener, S., Kirchhofer, D., Liu, I., Pyrdol, J., et al. (2020). Single-Cell RNA-Seq Reveals Cellular Hierarchies and Impaired Developmental Trajectories in Pediatric Ependymoma. Cancer Cell *38*, 44–59.e9. https://doi.org/10.1016/j.ccell.2020.06.004.
13. Couturier, C.P., Ayyadhury, S., Le, P.U., Nadaf, J., Monlong, J., Riva, G., Allache, R., Baig, S., Yan, X., Bourgey, M., et al. (2020). Single-cell RNA-seq reveals that glioblastoma recapitulates a normal neurodevelopmental hierarchy. Nat. Commun. *11*, 3406. https://doi.org/10.1038/s41467-020-17186-5.
14. Jessa, S., Blanchet-Cohen, A., Krug, B., Vladoiu, M., Coutelier, M., Faury, D., Poreau, B., De Jay, N., Hébert, S., Monlong, J., et al. (2019). Stalled developmental programs at the root of pediatric brain tumors. Nat. Genet. *51*, 1702–1713. https://doi.org/10.1038/s41588-019-0531-7.

15. Jessa, S., Mohammadnia, A., Harutyunyan, A.S., Hulswit, M., Varadharajan, S., Lakkis, H., Kabir, N., Bashardanesh, Z., Hébert, S., Faury, D., et al. (2022). K27M in canonical and noncanonical H3 variants occurs in distinct oligodendroglial cell lineages in brain midline gliomas. Nat. Genet. *54*, 1865–1880. https://doi.org/10.1038/s41588-022-01205-w.

16. Filbin, M.G., Tirosh, I., Hovestadt, V., Shaw, M.L., Escalante, L.E., Mathewson, N.D., Neftel, C., Frank, N., Pelton, K., Hebert, C.M., et al. (2018). Developmental and oncogenic programs in H3K27M gliomas dissected by single-cell RNA-seq. Science *360*, 331–335. https://doi.org/10.1126/science.aao4750.

17. Harpaz, N., Mittelman, T., Beresh, O., Griess, O., Furth, N., Salame, T.-M., Oren, R., Fellus-Alyagor, L., Harmelin, A., Alexandrescu, S., et al. (2022). Single-cell epigenetic analysis reveals principles of chromatin states in H3.3-K27M gliomas. Mol. Cell *82*, 2696–2713.e9. https://doi.org/10.1016/j.molcel.2022.05.023.

18. Garofano, L., Migliozzi, S., Oh, Y.T., D'Angelo, F., Najac, R.D., Ko, A., Frangaj, B., Caruso, F.P., Yu, K., Yuan, J., et al. (2021). Pathway-based classification of glioblastoma uncovers a mitochondrial subtype with therapeutic vulnerabilities. Nat. Cancer *2*, 141–156. https://doi.org/10.1038/s43018-020-00159-4.

19. Liu, I., Jiang, L., Samuelsson, E.R., Marco Salas, S., Beck, A., Hack, O.A., Jeong, D., Shaw, M.L., Englinger, B., LaBelle, J., et al. (2022). The landscape of tumor cell states and spatial organization in H3-K27M mutant diffuse midline glioma across age and location. Nat. Genet. *54*, 1881–1894. https://doi.org/10.1038/s41588-022-01236-3.

20. Karimi, E., Yu, M.W., Maritan, S.M., Perus, L.J.M., Rezanejad, M., Sorin, M., Dankner, M., Fallah, P., Doré, S., Zuo, D., et al. (2023). Single-cell spatial immune landscapes of primary and metastatic brain tumours. Nature *614*, 555–563. https://doi.org/10.1038/s41586-022-05680-3.

21. Chen, C.C.L., Deshmukh, S., Jessa, S., Hadjadj, D., Lisi, V., Andrade, A.F., Faury, D., Jawhar, W., Dali, R., Suzuki, H., et al. (2020). Histone H3.3G34-Mutant Interneuron Progenitors Co-opt PDGFRA for Gliomagenesis. Cell *183*, 1617–1633.e22. https://doi.org/10.1016/j.cell.2020.11.012.

22. Wang, L., Jung, J., Babikir, H., Shamardani, K., Jain, S., Feng, X., Gupta, N., Rosi, S., Chang, S., Raleigh, D., et al. (2022). A single-cell atlas of glioblastoma evolution under therapy reveals cell-intrinsic and cell-extrinsic therapeutic targets. Nat. Cancer *3*, 1534–1552. https://doi.org/10.1038/s43018-022-00475-x.

23. DeSisto, J., Donson, A.M., Griesinger, A.M., Fu, R., Riemondy, K., Mulcahy Levy, J., Siegenthaler, J.A., Foreman, N.K., Vibhakar, R., and Green, A.L. (2024). Tumor and immune cell types interact to produce heterogeneous phenotypes of pediatric high-grade glioma. Neuro Oncol. *26*, 538–552. https://doi.org/10.1093/neuonc/noad207.

24. LaBelle, J.J., Haase, R.D., Beck, A., Haase, J., Jiang, L., Oliveira de Biagi, C.A., Neyazi, S., Englinger, B., Liu, I., Trissal, M., et al. (2025). Dissecting the immune landscape in pediatric high-grade glioma reveals cell state changes under therapeutic pressure. Cell Rep. Med. *6*, 102095. https://doi.org/10.1016/j.xcrm.2025.102095.

25. Andrade, A.F., Annett, A., Karimi, E., Topouza, D.G., Rezanejad, M., Liu, Y., McNicholas, M., Gonzalez Santiago, E.G., Llivichuzhca-Loja, D., Gehlhaar, A., et al. (2024). Immune landscape of oncohistone-mutant gliomas reveals diverse myeloid populations and tumor-promoting function. Nat. Commun. *15*, 7769. https://doi.org/10.1038/s41467-024-52096-w.

26. Spitzer, A., Johnson, K.C., Nomura, M., Garofano, L., Nehar-belaid, D., Darnell, N.G., Greenwald, A.C., Bussema, L., Oh, Y.T., Varn, F.S., et al. (2025). Deciphering the longitudinal trajectories of glioblastoma ecosystems by integrative single-cell genomics. Nat. Genet. *57*, 1168–1178. https://doi.org/10.1038/s41588-025-02168-4.

27. Nomura, M., Spitzer, A., Johnson, K.C., Garofano, L., Nehar-belaid, D., Galili Darnell, N., Greenwald, A.C., Bussema, L., Oh, Y.T., Varn, F.S., et al. (2025). The multilayered transcriptional architecture of glioblastoma ecosystems. Nat. Genet. *57*, 1155–1167. https://doi.org/10.1038/s41588-025-02167-5.

28. Sussman, J.H., Cillo, A.R., Kohli, S., Cardello, C., Patterson, J., Akca, E., Angione, A., Moon, D., Krueger, K., Ghamari, A., et al. (2026). Single-cell profiling of peripheral and local immune compartments reveal unique genotype-independent prognostic immune signatures across isocitrate dehydrogenase-stratified glioma. Neuro Oncol. *28*, 143–158. https://doi.org/10.1093/neuonc/noaf206.

29. Varn, F.S., Johnson, K.C., Martinek, J., Huse, J.T., Nasrallah, M.P., Wesseling, P., Cooper, L.A.D., Malta, T.M., Wade, T.E., Sabedot, T.S., et al. (2022). Glioma progression is shaped by genetic evolution and microenvironment interactions. Cell *185*, 2184–2199.e16. https://doi.org/10.1016/j.cell.2022.04.038.

30. Aubin, R.G., Troisi, E.C., Montelongo, J., Alghalith, A.N., Nasrallah, M.P., Santi, M., and Camara, P.G. (2022). Pro-inflammatory cytokines mediate the epithelial-to-mesenchymal-like transition of pediatric posterior fossa ependymoma. Nat. Commun. *13*, 3936. https://doi.org/10.1038/s41467-022-31683-9.

31. Suvà, M.L., and Tirosh, I. (2020). The Glioma Stem Cell Model in the Era of Single-Cell Genomics. Cancer Cell *37*, 630–636. https://doi.org/10.1016/j.ccell.2020.04.001.

32. Sussman, J.H., Xu, J., Amankulor, N., and Tan, K. (2023). Dissecting the tumor microenvironment of epigenetically-driven gliomas: Opportunities for single-cell and spatial multiomics. Neuro-Oncol. Adv *5*, vdad101. https://doi.org/10.1093/noajnl/vdad101.

33. Spitzer, A., Gritsch, S., Nomura, M., Jucht, A., Fortin, J., Raviram, R., Weisman, H.R., Gonzalez Castro, L.N., Druck, N., Chanoch-Myers, R., et al. (2024). Mutant IDH inhibitors induce lineage differentiation in IDH-mutant oligodendroglioma. Cancer Cell *42*, 904–914.e9. https://doi.org/10.1016/j.ccell.2024.03.008.

34. Johnson, K.C., Anderson, K.J., Courtois, E.T., Gujar, A.D., Barthel, F.P., Varn, F.S., Luo, D., Seignon, M., Yi, E., Kim, H., et al. (2021). Single-cell multimodal glioma analyses identify epigenetic regulators of cellular plasticity and environmental stress response. Nat. Genet. *53*, 1456–1468. https://doi.org/10.1038/s41588-021-00926-8.

35. Liu, I., Alencastro Veiga Cruzeiro, G., Bjerke, L., Rogers, R.F., Grabovska, Y., Beck, A., Mackay, A., Barron, T., Hack, O.A., Quezada, M.A., et al. (2024). GABAergic neuronal lineage development determines clinically actionable targets in diffuse hemispheric glioma, H3G34-mutant. Cancer Cell *42*, 1528–1548.e17. https://doi.org/10.1016/j.ccell.2024.08.006.

36. Lilly, J.V., Rokita, J.L., Mason, J.L., Patton, T., Stefankiewiz, S., Higgins, D., Trooskin, G., Larouci, C.A., Arya, K., Appert, E., et al. (2023). The children's brain tumor network (CBTN) - Accelerating research in pediatric central nervous system tumors through collaboration and open science. Neoplasia *35*, 100846. https://doi.org/10.1016/j.neo.2022.100846.

37. Shapiro, J.A., Gaonkar, K.S., Spielman, S.J., Savonen, C.L., Bethell, C.J., Jin, R., Rathi, K.S., Zhu, Y., Egolf, L.E., Farrow, B.K., et al. (2023). OpenPBTA: The Open Pediatric Brain Tumor Atlas. Cell Genom. *3*, 100340. https://doi.org/10.1016/j.xgen.2023.100340.

38. Schep, A.N., Wu, B., Buenrostro, J.D., and Greenleaf, W.J. (2017). chromVAR: inferring transcription-factor-associated accessibility from single-cell epigenomic data. Nat. Methods *14*, 975–978. https://doi.org/10.1038/nmeth.4401.

39. Marques, C., Unterkircher, T., Kroon, P., Oldrini, B., Izzo, A., Dramaretska, Y., Ferrarese, R., Kling, E., Schnell, O., Nelander, S., et al. (2021). NF1 regulates mesenchymal glioblastoma plasticity and aggressiveness through the AP-1 transcription factor FOSL1. eLife *10*, e64846. https://doi.org/10.7554/eLife.64846.

40. Zhao, K., Cui, X., Wang, Q., Fang, C., Tan, Y., Wang, Y., Yi, K., Yang, C., You, H., Shang, R., et al. (2019). RUNX1 contributes to the mesenchymal subtype of glioblastoma in a TGFβ pathway-dependent manner. Cell Death Dis. *10*, 877. https://doi.org/10.1038/s41419-019-2108-x.

41. Dimitrov, D., Türei, D., Garrido-Rodriguez, M., Burmedi, P.L., Nagai, J.S., Boys, C., Ramirez Flores, R.O., Kim, H., Szalai, B., Costa, I.G., et al.

(2022). Comparison of methods and resources for cell-cell communication inference from single-cell RNA-Seq data. Nat. Commun. *13*, 3224. https://doi.org/10.1038/s41467-022-30755-0.

42. Ma, R.-Y., Black, A., and Qian, B.-Z. (2022). Macrophage diversity in cancer revisited in the era of single-cell omics. Trends Immunol. *43*, 546–563. https://doi.org/10.1016/j.it.2022.04.008.
43. Cheng, S., Li, Z., Gao, R., Xing, B., Gao, Y., Yang, Y., Qin, S., Zhang, L., Ouyang, H., Du, P., et al. (2021). A pan-cancer single-cell transcriptional atlas of tumor infiltrating myeloid cells. Cell *184*, 792–809.e23. https://doi.org/10.1016/j.cell.2021.01.010.
44. Gupta, P., Dang, M., Oberai, S., Migliozzi, S., Trivedi, R., Kumar, G., Peshoff, M., Milam, N., Ahmed, A., Bojja, K., et al. (2024). Immune landscape of isocitrate dehydrogenase-stratified primary and recurrent human gliomas. Neuro Oncol. *26*, 2239–2255. https://doi.org/10.1093/neuonc/noae139.
45. Abdelfattah, N., Kumar, P., Wang, C., Leu, J.-S., Flynn, W.F., Gao, R., Baskin, D.S., Pichumani, K., Ijare, O.B., Wood, S.L., et al. (2022). Single-cell analysis of human glioma and immune cells identifies S100A4 as an immunotherapy target. Nat. Commun. *13*, 767. https://doi.org/10.1038/s41467-022-28372-y.
46. Masuda, T., Sankowski, R., Staszewski, O., Böttcher, C., Amann, L., van Loo, G., Scheiwe, C., Scheiwe, C., Nessler, S., Kunz, P., et al. (2019). Spatial and temporal heterogeneity of mouse and human microglia at single-cell resolution. Nature *566*, 388–392. https://doi.org/10.1038/s41586-019-0924-x.
47. Masuda, T., Sankowski, R., Staszewski, O., and Prinz, M. (2020). Microglia Heterogeneity in the Single-Cell Era. Cell Rep. *30*, 1271–1281. https://doi.org/10.1016/j.celrep.2020.01.010.
48. Hara, T., Chanoch-Myers, R., Mathewson, N.D., Myskiw, C., Atta, L., Bussema, L., Eichhorn, S.W., Greenwald, A.C., Kinker, G.S., Rodman, C., et al. (2021). Interactions between cancer cells and immune cells drive transitions to mesenchymal-like states in glioblastoma. Cancer Cell *39*, 779–792.e11. https://doi.org/10.1016/j.ccell.2021.05.002.
49. Kolliopoulos, C., Ali, M.M., Castillejo-Lopez, C., Heldin, C.-H., and Heldin, P. (2022). CD44 Depletion in Glioblastoma Cells Suppresses Growth and Stemness and Induces Senescence. Cancers *14*, 3747. https://doi.org/10.3390/cancers14153747.
50. Mooney, K.L., Choy, W., Sidhu, S., Pelargos, P., Bui, T.T., Voth, B., Barnette, N., and Yang, I. (2016). The role of CD44 in glioblastoma multiforme. J. Clin. Neurosci. *34*, 1–5. https://doi.org/10.1016/j.jocn.2016.05.012.
51. Xiao, Y., Yang, K., Wang, Z., Zhao, M., Deng, Y., Ji, W., Zou, Y., Qian, C., Liu, Y., Xiao, H., and Liu, H. (2021). CD44-Mediated Poor Prognosis in Glioma Is Associated With M2-Polarization of Tumor-Associated Macrophages and Immunosuppression. Front. Surg. *8*, 775194. https://doi.org/10.3389/fsurg.2021.775194.
52. Jin, S., Guerrero-Juarez, C.F., Zhang, L., Chang, I., Ramos, R., Kuan, C.H., Myung, P., Plikus, M.V., and Nie, Q. (2021). Inference and analysis of cell-cell communication using CellChat. Nat. Commun. *12*, 1088. https://doi.org/10.1038/s41467-021-21246-9.
53. Ren, Y., Huang, Z., Zhou, L., Xiao, P., Song, J., He, P., Xie, C., Zhou, R., Li, M., Dong, X., et al. (2023). Spatial transcriptomics reveals niche-specific enrichment and vulnerabilities of radial glial stem-like cells in malignant gliomas. Nat. Commun. *14*, 1028. https://doi.org/10.1038/s41467-023-36707-6.
54. Shekarian, T., Zinner, C.P., Bartoszek, E.M., Duchemin, W., Wachnowicz, A.T., Hogan, S., Etter, M.M., Flammer, J., Paganetti, C., Martins, T.A., et al. (2022). Immunotherapy of glioblastoma explants induces interferon-γ responses and spatial immune cell rearrangements in tumor center, but not periphery. Sci. Adv. *8*, eabn9440. https://doi.org/10.1126/sciadv.abn9440.
55. Zheng, Y., Carrillo-Perez, F., Pizurica, M., Heiland, D.H., and Gevaert, O. (2023). Spatial cellular architecture predicts prognosis in glioblastoma. Nat. Commun. *14*, 4122. https://doi.org/10.1038/s41467-023-39933-0.
56. Ravi, V.M., Will, P., Kueckelhaus, J., Sun, N., Joseph, K., Salié, H., Vollmer, L., Kuliesiute, U., von Ehr, J., Benotmane, J.K., et al. (2022). Spatially resolved multi-omics deciphers bidirectional tumor-host interdependence in glioblastoma. Cancer Cell *40*, 639–655.e13. https://doi.org/10.1016/j.ccell.2022.05.009.
57. Klemm, F., Maas, R.R., Bowman, R.L., Kornete, M., Soukup, K., Nassiri, S., Brouland, J.-P., Iacobuzio-Donahue, C.A., Brennan, C., Tabar, V., et al. (2020). Interrogation of the Microenvironmental Landscape in Brain Tumors Reveals Disease-Specific Alterations of Immune Cells. Cell *181*, 1643–1660.e17. https://doi.org/10.1016/j.cell.2020.05.007.
58. Greenwald, A.C., Darnell, N.G., Hoefflin, R., Simkin, D., Mount, C.W., Gonzalez Castro, L.N., Harnik, Y., Dumont, S., Hirsch, D., Nomura, M., et al. (2024). Integrative spatial analysis reveals a multi-layered organization of glioblastoma. Cell *187*, 2485–2501.e26. https://doi.org/10.1016/j.cell.2024.03.029.
59. Xiong, B., Hu, Y., and Tan, K. (2025). N-Orbit: towards a universal model and metric for comparing tissue microenvironments. preprint at bioRxiv. https://doi.org/10.1101/2025.04.23.650192.
60. Wu, C.-Y., Rong, J., Sathe, A., Hess, P.R., Lau, B.T., Grimes, S.M., Huang, S., Ji, H.P., and Zhang, N.R. (2025). Cancer subclone detection based on DNA copy number in single-cell and spatial omic sequencing data. Nat. Methods *22*, 1846–1856. https://doi.org/10.1038/s41592-025-02773-5.
61. Venkatesh, H.S., Morishita, W., Geraghty, A.C., Silverbush, D., Gillespie, S.M., Arzt, M., Tam, L.T., Espenel, C., Ponnuswami, A., Ni, L., et al. (2019). Electrical and synaptic integration of glioma into neural circuits. Nature *573*, 539–545. https://doi.org/10.1038/s41586-019-1563-y.
62. Taylor, K.R., Barron, T., Hui, A., Spitzer, A., Yalçin, B., Ivec, A.E., Geraghty, A.C., Hartmann, G.G., Arzt, M., Gillespie, S.M., et al. (2023). Glioma synapses recruit mechanisms of adaptive plasticity. Nature *623*, 366–374. https://doi.org/10.1038/s41586-023-06678-1.
63. Sun, Y., Wang, X., Zhang, D.Y., Zhang, Z., Bhattarai, J.P., Wang, Y., Park, K.H., Dong, W., Hung, Y.F., Yang, Q., et al. (2025). Brain-wide neuronal circuit connectome of human glioblastoma. Nature *641*, 222–231. https://doi.org/10.1038/s41586-025-08634-7.
64. Sun, M.A., Yang, R., Liu, H., Wang, W., Song, X., Hu, B., Reynolds, N., Roso, K., Chen, L.H., Greer, P.K., et al. (2023). Repurposing Clemastine to Target Glioblastoma Cell Stemness. Cancers *15*, 4619. https://doi.org/10.3390/cancers15184619.
65. Thompson, E.G., and Sontheimer, H. (2019). Acetylcholine Receptor Activation as a Modulator of Glioblastoma Invasion. Cells *8*, 1203. https://doi.org/10.3390/cells8101203.
66. Zhang, B., Zhao, J., Wang, Y., Xu, H., Gao, B.O., Zhang, G., Han, B., Song, G., Zhang, J., and Meng, W. (2023). CHRM3 is a novel prognostic factor of poor prognosis and promotes glioblastoma progression via activation of oncogenic invasive growth factors. Oncol. Res. *31*, 917–927. https://doi.org/10.32604/or.2023.030425.
67. Caragher, S.P., Shireman, J.M., Huang, M., Miska, J., Atashi, F., Baisiwala, S., Hong Park, C., Saathoff, M.R., Warnke, L., Xiao, T., et al. (2019). Activation of Dopamine Receptor 2 Prompts Transcriptomic and Metabolic Plasticity in Glioblastoma. J. Neurosci. *39*, 1982–1993. https://doi.org/10.1523/JNEUROSCI.1589-18.2018.
68. Jeon, H.-M., Oh, Y.T., Shin, Y.J., Chang, N., Kim, D., Woo, D., Yeup, Y., Joo, K.M., Jo, H., Yang, H., et al. (2023). Dopamine receptor D2 regulates glioblastoma survival and death through MET and death receptor 4/5. Neoplasia *39*, 100894. https://doi.org/10.1016/j.neo.2023.100894.
69. Liu, B., Shi, Y., Qin, B., Cheng, D., Nie, Z., Zhai, H., Li, Y., Jin, Z., Pu, J., Yan, D., et al. (2023). Sertindole inhibits autophagic flux and glioma progression. MedComm – Oncol *2*, e41. https://doi.org/10.1002/mog2.41.
70. Barron, T., Yalçın, B., Su, M., Byun, Y.G., Gavish, A., Shamardani, K., Xu, H., Ni, L., Soni, N., Mehta, V., et al. (2025). GABAergic neuron-to-glioma synapses in diffuse midline gliomas. Nature *639*, 1060–1068. https://doi.org/10.1038/s41586-024-08579-3.

71. Blanchart, A., Fernando, R., Häring, M., Assaife-Lopes, N., Romanov, R.A., Andäng, M., Harkany, T., and Ernfors, P. (2017). Endogenous GABAA receptor activity suppresses glioma growth. Oncogene *36*, 777–786. https://doi.org/10.1038/onc.2016.245.

72. Smits, A., Jin, Z., Elsir, T., Pedder, H., Nistér, M., Alafuzoff, I., Dimberg, A., Edqvist, P.-H., Pontén, F., Aronica, E., and Birnir, B. (2012). GABA-A Channel Subunit Expression in Human Glioma Correlates with Tumor Histology and Clinical Outcome. PLoS One *7*, e37041. https://doi.org/10.1371/journal.pone.0037041.

73. Murase, R., Taketomi, Y., Miki, Y., Nishito, Y., Saito, M., Fukami, K., Yamamoto, K., and Murakami, M. (2017). Group III phospholipase A2 promotes colitis and colorectal cancer. Sci. Rep. *7*, 12261. https://doi.org/10.1038/s41598-017-12434-z.

74. Miki, Y., Kidoguchi, Y., Sato, M., Taketomi, Y., Taya, C., Muramatsu, K., Gelb, M.H., Yamamoto, K., and Murakami, M. (2016). Dual Roles of Group IID Phospholipase A2 in Inflammation and Cancer. J. Biol. Chem. *291*, 15588–15601. https://doi.org/10.1074/jbc.M116.734624.

75. Yi, K., Zhan, Q., Wang, Q., Tan, Y., Fang, C., Wang, Y., Zhou, J., Yang, C., Li, Y., and Kang, C. (2021). PTRF/cavin-1 remodels phospholipid metabolism to promote tumor proliferation and suppress immune responses in glioblastoma by stabilizing cPLA2. Neuro Oncol. *23*, 387–399. https://doi.org/10.1093/neuonc/noaa255.

76. Zhang, H., Zhao, H., Wang, H., Yin, Z., Huang, K., and Yu, M. (2022). High PLA2 level is correlated with glioblastoma progression via regulating DNA replication. J. Cell Mol. Med. *26*, 1466–1472. https://doi.org/10.1111/jcmm.17140.

77. Hernández, M., Martín, R., García-Cubillas, M.D., Maeso-Hernández, P., and Nieto, M.L. (2010). Secreted PLA2 induces proliferation in astrocytoma through the EGF receptor: another inflammation-cancer link. Neuro Oncol. *12*, 1014–1023. https://doi.org/10.1093/neuonc/noq078.

78. Hao, Y., Hao, S., Andersen-Nissen, E., Mauck, W.M., Zheng, S., Butler, A., Lee, M.J., Wilk, A.J., Darby, C., Zager, M., et al. (2021). Integrated analysis of multimodal single-cell data. Cell *184*, 3573–3587.e29. https://doi.org/10.1016/j.cell.2021.04.048.

79. Hao, Y., Stuart, T., Kowalski, M.H., Choudhary, S., Hoffman, P., Hartman, A., Srivastava, A., Molla, G., Madad, S., Fernandez-Granda, C., and Satija, R. (2024). Dictionary learning for integrative, multimodal and scalable single-cell analysis. Nat. Biotechnol. *42*, 293–304. https://doi.org/10.1038/s41587-023-01767-y.

80. Stuart, T., Srivastava, A., Madad, S., Lareau, C.A., and Satija, R. (2021). Single-cell chromatin state analysis with Signac. Nat. Methods *18*, 1333–1341. https://doi.org/10.1038/s41592-021-01282-5.

81. McGinnis, C.S., Murrow, L.M., and Gartner, Z.J. (2019). DoubletFinder: Doublet Detection in Single-Cell RNA Sequencing Data Using Artificial Nearest Neighbors. Cell Syst. *8*, 329–337.e4. https://doi.org/10.1016/j.cels.2019.03.003.

82. Tirosh, I., Venteicher, A.S., Hebert, C., Escalante, L.E., Patel, A.P., Yizhak, K., Fisher, J.M., Rodman, C., Mount, C., Filbin, M.G., et al. (2016). Single-cell RNA-seq supports a developmental hierarchy in human oligodendroglioma. Nature *539*, 309–313. https://doi.org/10.1038/nature20123.

83. Trapnell, C., Cacchiarelli, D., Grimsby, J., Pokharel, P., Li, S., Morse, M., Lennon, N.J., Livak, K.J., Mikkelsen, T.S., and Rinn, J.L. (2014). The dynamics and regulators of cell fate decisions are revealed by pseudotemporal ordering of single cells. Nat. Biotechnol. *32*, 381–386. https://doi.org/10.1038/nbt.2859.

84. La Manno, G., Soldatov, R., Zeisel, A., Braun, E., Hochgerner, H., Petukhov, V., Lidschreiber, K., Kastriti, M.E., Lönnerberg, P., Furlan, A., et al. (2018). RNA velocity of single cells. Nature *560*, 494–498. https://doi.org/10.1038/s41586-018-0414-6.

85. Wolf, F.A., Angerer, P., and Theis, F.J. (2018). SCANPY: large-scale single-cell gene expression data analysis. Genome Biol. *19*, 15. https://doi.org/10.1186/s13059-017-1382-0.

86. Greenwald, N.F., Miller, G., Moen, E., Kong, A., Kagel, A., Dougherty, T., Fullaway, C.C., McIntosh, B.J., Leow, K.X., Schwartz, M.S., et al. (2022). Whole-cell segmentation of tissue images with human-level performance using large-scale data annotation and deep learning. Nat. Biotechnol. *40*, 555–565. https://doi.org/10.1038/s41587-021-01094-0.

87. Bergen, V., Lange, M., Peidli, S., Wolf, F.A., and Theis, F.J. (2020). Generalizing RNA velocity to transient cell states through dynamical modeling. Nat. Biotechnol. *38*, 1408–1414. https://doi.org/10.1038/s41587-020-0591-3.

88. Morabito, S., Reese, F., Rahimzadeh, N., Miyoshi, E., and Swarup, V. (2023). hdWGCNA identifies co-expression networks in high-dimensional transcriptomics data. Cell Rep. Methods *3*, 100498. https://doi.org/10.1016/j.crmeth.2023.100498.

89. Yu, W., Uzun, Y., Zhu, Q., Chen, C., and Tan, K. (2020). scATAC-pro: a comprehensive workbench for single-cell chromatin accessibility sequencing data. Genome Biol. *21*, 94. https://doi.org/10.1186/s13059-020-02008-0.

90. Zhang, Y., Liu, T., Meyer, C.A., Eeckhoute, J., Johnson, D.S., Bernstein, B.E., Nusbaum, C., Myers, R.M., Brown, M., Li, W., and Liu, X.S. (2008). Model-based Analysis of ChIP-Seq (MACS). Genome Biol. *9*, R137. https://doi.org/10.1186/gb-2008-9-9-r137.

91. Yu, G., Wang, L.-G., Han, Y., and He, Q.-Y. (2012). clusterProfiler: an R Package for Comparing Biological Themes Among Gene Clusters. OMICS A J. Integr. Biol. *16*, 284–287. https://doi.org/10.1089/omi.2011.0118.

92. Law, C.W., Chen, Y., Shi, W., and Smyth, G.K. (2014). voom: precision weights unlock linear model analysis tools for RNA-seq read counts. Genome Biol. *15*, R29. https://doi.org/10.1186/gb-2014-15-2-r29.

93. Hoffman, G.E., and Roussos, P. (2021). Dream: powerful differential expression analysis for repeated measures designs. Bioinformatics *37*, 192–201. https://doi.org/10.1093/bioinformatics/btaa687.

94. Korotkevich, G., Sukhov, V., Budin, N., Shpak, B., Artyomov, M.N., and Sergushichev, A. (2021). Fast gene set enrichment analysis. preprint at bioRxiv. https://doi.org/10.1101/060012.

95. Sandmann, S., Inserte, C., and Varghese, J. (2022). clevRvis: visualization techniques for clonal evolution. GigaScience *12*, giad020. https://doi.org/10.1093/gigascience/giad020.

96. Aibar, S., González-Blas, C.B., Moerman, T., Huynh-Thu, V.A., Imrichova, H., Hulselmans, G., Rambow, F., Marine, J.-C., Geurts, P., Aerts, J., et al. (2017). SCENIC: single-cell regulatory network inference and clustering. Nat. Methods *14*, 1083–1086. https://doi.org/10.1038/nmeth.4463.

97. Newman, A.M., Steen, C.B., Liu, C.L., Gentles, A.J., Chaudhuri, A.A., Scherer, F., Khodadoust, M.S., Esfahani, M.S., Luca, B.A., Steiner, D., et al. (2019). Determining cell type abundance and expression from bulk tissues with digital cytometry. Nat. Biotechnol. *37*, 773–782. https://doi.org/10.1038/s41587-019-0114-2.

98. Windhager, J., Zanotelli, V.R.T., Schulz, D., Meyer, L., Daniel, M., Bodenmiller, B., and Eling, N. (2023). An end-to-end workflow for multiplexed image processing and analysis. Nat. Protoc. *18*, 3565–3613. https://doi.org/10.1038/s41596-023-00881-0.

99. Bankhead, P., Loughrey, M.B., Fernández, J.A., Dombrowski, Y., McArt, D.G., Dunne, P.D., McQuaid, S., Gray, R.T., Murray, L.J., Coleman, H.G., QuPath, et al. (2017). Open source software for digital pathology image analysis. Sci Rep. *7*, 16878. https://doi.org/10.1038/s41598-017-17204-5.

100. McInnes, L., Healy, J., and Astels, S. (2017). hdbscan: Hierarchical density based clustering. J. Open Source Softw. *2*, 205. https://doi.org/10.21105/joss.00205.

101. Ijaz, H., Koptyra, M., Gaonkar, K.S., Rokita, J.L., Baubet, V.P., Tauhid, L., Zhu, Y., Brown, M., Lopez, G., Zhang, B., et al. (2020). Pediatric high-grade glioma resources from the Children's Brain Tumor Tissue

Consortium. Neuro Oncol. *22*, 163–165. https://doi.org/10.1093/neuonc/noz192.

102. Chen, X., Schulz-Trieglaff, O., Shaw, R., Barnes, B., Schlesinger, F., Källberg, M., Cox, A.J., Kruglyak, S., and Saunders, C.T. (2016). Manta: rapid detection of structural variants and indels for germline and cancer sequencing applications. Bioinformatics *32*, 1220–1222. https://doi.org/10.1093/bioinformatics/btv710.

103. Van der Auwera, G.A., Carneiro, M.O., Hartl, C., Poplin, R., Del Angel, G., Levy-Moonshine, A., Jordan, T., Shakir, K., Roazen, D., Thibault, J., et al. (2013). From FastQ data to high confidence variant calls: the Genome Analysis Toolkit best practices pipeline. Curr. Protoc. Bioinforma. *43*, 11. https://doi.org/10.1002/0471250953.bi1110s43.

104. Kim, S., Scheffler, K., Halpern, A.L., Bekritsky, M.A., Noh, E., Källberg, M., Chen, X., Kim, Y., Beyter, D., Krusche, P., and Saunders, C.T. (2018). Strelka2: fast and accurate calling of germline and somatic variants. Nat. Methods *15*, 591–594. https://doi.org/10.1038/s41592-018-0051-x.

105. Sondka, Z., Dhir, N.B., Carvalho-Silva, D., Jupe, S., Ahmed, M., , et al.McLaren, K., McLaren, K., Starkey, M., Ward, S., Wilding, J. (2024). COSMIC: a curated database of somatic variants and clinical data for cancer. Nucleic Acids Res. *52*, D1210–D1217. https://doi.org/10.1093/nar/gkad986.

106. Sill, M., Schrimpf, D., Patel, A., Sturm, D., Jäger, N., Sievers, P., Schweizer, L., Banan, R., Reuss, D., Suwala, A., et al. (2026). Advancing CNS tumor diagnostics with expanded DNA methylation-based classification. Cancer Cell *44*, 340–354.e2. https://doi.org/10.1016/j.ccell.2025.11.002.

107. Cao, J., Spielmann, M., Qiu, X., Huang, X., Ibrahim, D.M., Hill, A.J., Zhang, F., Mundlos, S., Christiansen, L., Steemers, F.J., et al. (2019). The single-cell transcriptional landscape of mammalian organogenesis. Nature *566*, 496–502. https://doi.org/10.1038/s41586-019-0969-x.

108. Liberzon, A., Birger, C., Thorvaldsdóttir, H., Ghandi, M., Mesirov, J.P., and Tamayo, P. (2015). The Molecular Signatures Database (MSigDB) hallmark gene set collection. Cell Syst. *1*, 417–425. https://doi.org/10.1016/j.cels.2015.12.004.

109. Kanehisa, M., Furumichi, M., Tanabe, M., Sato, Y., and Morishima, K. (2017). KEGG: new perspectives on genomes, pathways, diseases and drugs. Nucleic Acids Res. *45*, D353–D361. https://doi.org/10.1093/nar/gkw1092.

110. Stuart, T., Butler, A., Hoffman, P., Hafemeister, C., Papalexi, E., Mauck, W.M., Hao, Y., Stoeckius, M., Smibert, P., and Satija, R. (2019). Comprehensive Integration of Single-Cell Data. Cell *177*, 1888–1902.e21. https://doi.org/10.1016/j.cell.2019.05.031.

111. Chen, C., Yu, W., Alikarami, F., Qiu, Q., Chen, C.H., Flournoy, J., Gao, P., Uzun, Y., Fang, L., Davenport, J.W., et al. (2022). Single-cell multiomics reveals increased plasticity, resistant populations, and stem-cell–like blasts in KMT2A-rearranged leukemia. Blood *139*, 2198–2211. https://doi.org/10.1182/blood.2021013442.

112. Hou, R., Denisenko, E., Ong, H.T., Ramilowski, J.A., and Forrest, A.R.R. (2020). Predicting cell-to-cell communication networks using NATMI. Nat. Commun. *11*, 5011. https://doi.org/10.1038/s41467-020-18873-z.

113. Raredon, M.S.B., Yang, J., Garritano, J., Wang, M., Kushnir, D., Schupp, J.C., Adams, T.S., Greaney, A.M., Leiby, K.L., Kaminski, N., et al. (2022). Computation and visualization of cell–cell signaling topologies in single-cell systems data using Connectome. Sci. Rep. *12*, 4187. https://doi.org/10.1038/s41598-022-07959-x.

114. Cabello-Aguilar, S., Alame, M., Kon-Sun-Tack, F., Fau, C., Lacroix, M., and Colinge, J. (2020). SingleCellSignalR: inference of intercellular networks from single-cell transcriptomics. Nucleic Acids Res. *48*, e55. https://doi.org/10.1093/nar/gkaa183.

115. Efremova, M., Vento-Tormo, M., Teichmann, S.A., and Vento-Tormo, R. (2020). CellPhoneDB: inferring cell–cell communication from combined expression of multi-subunit ligand–receptor complexes. Nat. Protoc. *15*, 1484–1506. https://doi.org/10.1038/s41596-020-0292-x.

116. Ruiz-Moreno, C., Salas, S.M., Samuelsson, E., Minaeva, M., Ibarra, I., Grillo, M., Brandner, S., Roy, A., Forsberg-Nilsson, K., Kranendonk, M.E.G., et al. (2025). Charting the single-cell and spatial landscape of IDH-wild-type glioblastoma with GBmap. Neuro Oncol. *27*, 2281–2295. https://doi.org/10.1093/neuonc/noaf113.

117. Müller, S., Kohanbash, G., Liu, S.J., Alvarado, B., Carrera, D., Bhaduri, A., Watchmaker, P.B., Yagnik, G., Di Lullo, E., Malatesta, M., et al. (2017). Single-cell profiling of human gliomas reveals macrophage ontogeny as a basis for regional differences in macrophage activation in the tumor microenvironment. Genome Biol. *18*, 234. https://doi.org/10.1186/s13059-017-1362-4.

118. Van de Sande, B., Flerin, C., Davie, K., De Waegeneer, M., Hulselmans, G., Aibar, S., Seurinck, R., Saelens, W., Cannoodt, R., Rouchon, Q., et al. (2020). A scalable SCENIC workflow for single-cell gene regulatory network analysis. Nat. Protoc. *15*, 2247–2276. https://doi.org/10.1038/s41596-020-0336-2.

119. Schürch, C.M., Bhate, S.S., Barlow, G.L., Phillips, D.J., Noti, L., Zlobec, I., Chu, P., Black, S., Demeter, J., McIlwain, D.R., et al. (2020). Coordinated Cellular Neighborhoods Orchestrate Antitumoral Immunity at the Colorectal Cancer Invasive Front. Cell *182*, 1341–1359.e19. https://doi.org/10.1016/j.cell.2020.07.005.

120. Baddeley, A., and Turner, R. (2005). spatstat: An R Package for Analyzing Spatial Point Patterns. J. Stat. Softw. *12*, 1–42. https://doi.org/10.18637/jss.v012.i06.

121. Fang, R., Xia, C., Close, J.L., Zhang, M., He, J., Huang, Z., Halpern, A.R., Long, B., Miller, J.A., Lein, E.S., and Zhuang, X. (2022). Conservation and divergence of cortical cell organization in human and mouse revealed by MERFISH. Science *377*, 56–62. https://doi.org/10.1126/science.abm1741.

122. Zhang, M., Pan, X., Jung, W., Halpern, A.R., Eichhorn, S.W., Lei, Z., Cohen, L., Smith, K.A., Tasic, B., Yao, Z., et al. (2023). Molecularly defined and spatially resolved cell atlas of the whole mouse brain. Nature *624*, 343–354. https://doi.org/10.1038/s41586-023-06808-9.

123. Chen, X., Ji, Z.L., and Chen, Y.Z. (2002). TTD: Therapeutic Target Database. Nucleic Acids Res. *30*, 412–415.

124. Freshour, S.L., Kiwala, S., Cotto, K.C., Coffman, A.C., McMichael, J.F., Song, J.J., Griffith, M., Griffith, O.L., and Wagner, A.H. (2021). Integration of the Drug–Gene Interaction Database (DGIdb 4.0) with open crowdsource efforts. Nucleic Acids Res. *49*, D1144–D1151. https://doi.org/10.1093/nar/gkaa1084.

125. Koscielny, G., An, P., Carvalho-Silva, D., Cham, J.A., Fumis, L., Gasparyan, R., Hasan, S., Karamanis, N., Maguire, M., Papa, E., et al. (2017). Open Targets: a platform for therapeutic target identification and validation. Nucleic Acids Res. *45*, D985–D994. https://doi.org/10.1093/nar/gkw1055.

126. Subramanian, A., Narayan, R., Corsello, S.M., Peck, D.D., Natoli, T.E., Lu, X., Gould, J., Davis, J.F., Tubelli, A.A., Asiedu, J.K., et al. (2017). A Next Generation Connectivity Map: L1000 platform and the first 1,000,000 profiles. Cell *171*, 1437–1452.e17. https://doi.org/10.1016/j.cell.2017.10.049.

127. Tsherniak, A., Vazquez, F., Montgomery, P.G., Weir, B.A., Kryukov, G., Cowley, G.S., Gill, S., Harrington, W.F., Pantel, S., Krill-Burger, J.M., et al. (2017). Defining a Cancer Dependency Map. Cell *170*, 564–576.e16. https://doi.org/10.1016/j.cell.2017.06.010.

128. Zheng, S., Wang, W., Aldahdooh, J., Malyutina, A., Shadbahr, T., Tanoli, Z., Pessia, A., and Tang, J. (2022). SynergyFinder Plus: Toward Better Interpretation and Annotation of Drug Combination Screening Datasets. Genom. Proteom. Bioinform. *20*, 587–596. https://doi.org/10.1016/j.gpb.2022.01.004.

129. Love, M.I., Huber, W., and Anders, S. (2014). Moderated estimation of fold change and dispersion for RNA-seq data with DESeq2. Genome Biol. *15*, 550. https://doi.org/10.1186/s13059-014-0550-8.

STAR★METHODS

KEY RESOURCES TABLE

REAGENT or RESOURCE	SOURCE	IDENTIFIER
Antibodies		
Anti-CD31 (clone EP3095)	Akoya	4450017; RRID: AB_2915935
Anti-GLUT1 (clone EPR3915)	Abcam	ab252403; RRID: AB_3719889
Anti-CD4 (clone EPR6855)	Akoya	4550112; RRID: AB_3094499
Anti-CD44 (clone 156-3C11)	Akoya	4450041: RRID: AB_2936081
Anti-TMEM119 (clone CL8714)	Novus Biologicals	NBP2-76985, custom carrier-free
Anti-PAX5 (clone D7H5X)	Cell Signaling Technology	93009SF; RRID: AB_2798001
Anti-SOX4 (clone R807.1.1D6)	CDI Labs	MAB409325
Anti-CD206 (clone polyclonal)	R&D Systems	AF2534; RRID: AB_2063019
Anti-P53 (clone E26)	Abcam	ab225531; RRID: AB_3718659
Anti-CD68 (clone KP1)	Akoya	4550113; RRID: AB_2935894
Anti-PDGFRα (clone D13C6)	Cell Signaling Technology	26899SF
Anti-ATRX (clone polyclonal)	Atlas Antibodies	HPA001906, custom carrier-free; RRID: AB_1078249
Anti-GFAP (clone 2.2B10)	ThermoFisher	13–0300; RRID: AB_2532994
Anti-CD16 (clone D1N9L)	Cell Signaling Technology	72204SF; RRID: AB_3280014
Anti-VIM (clone 091D3)	Akoya	4450050; RRID: AB_2935889
Anti-CD11b (clone EPR1344)	Abcam	ab216445; RRID: AB_2864378
Anti-H3K27M (clone RM192)	RevMab	31-1175-00, custom carrier-free; RRID: AB_2316432
Anti-CD8 (clone C8/144B)	Akoya	4250012; RRID: AB_2915960
Anti-CD56 (clone CAL53)	Akoya	4250087; RRID: AB_2936082
Anti-PD-L1 (clone 73–10)	Abcam	ab226766; RRID: AB_3073663
Anti-CD133 (clone D2V8Q)	Cell Signaling Technology	51917SF; RRID: AB_3717833
Anti-FOXP3 (clone 236A/E7)	Akoya	4550071; RRID: AB_2927679
Anti-EGFR (clone D38B1)	Cell Signaling Technology	26038SF
Anti-HLA-DR (clone EPR3692)	Akoya	4550118; RRID: AB_3080864
Anti-OLIG2 (clone EPR2673)	Abcam	ab220796: RRID: AB_2923001
Anti-APOE (clone D7I9N)	Cell Signaling Technology	10197SF
Anti-PCNA (clone PC10)	Akoya	4550124; RRID: AB_2936083
Anti-CD14 (clone EPR3653)	Akoya	4450047; RRID: AB_3083457
Anti-MOG (clone EP4281)	Abcam	ab233025; RRID: AB_10863418
Anti-S100B (clone EP1576Y)	Abcam	ab215989; RRID: AB_3073612
Anti-Collagen IV (clone EPR209660)	Akoya	4550122; RRID: AB_2927676
Anti-CD3e (clone EP449E)	Akoya	4550119; RRID: AB_2936080
Anti-PD1 (clone D4W2J)	Akoya	4550038; RRID: AB_3096407
Anti-Ki-67 (clone B56)	Akoya	4250019; RRID: AB_2895046
Anti-CD47 (clone polyclonal)	R&D Systems	AF4670; RRID: AB_1026196
Anti-CX3CR1 (clone polyclonal)	Novus Biologicals	NBP1-76949
Anti-NeuN (clone EPR12763)	Abcam	ab209898; RRID: AB_3695640
Anti-P2RY12 (clone polyclonal)	Anaspec	AS-55042A, custom carrier-free; RRID: AB_2861284
Anti-IBA1 (clone LB1-6G11)	CDI Labs	MAB280995
Anti-CD163 (clone EPR19518)	Akoya	Akoya in-house custom order; RRID: AB_2935895
Anti-HIF-1α (clone EP1215Y)	Akoya	4550069; RRID: AB_3082972
Anti-Nestin (clone 196908)	R&D Systems	MAB1259; RRID: AB_2251304
Anti-SPP1 (clone EPR21139-316)	Abcam	ab236213; RRID: AB_2894860

(*Continued on next page*)

Continued

REAGENT or RESOURCE	SOURCE	IDENTIFIER
Anti-CD38 (clone E7Z8C)	Akoya	4250080; RRID: AB_3082976
Anti-CD79a (clone D1X5C)	Akoya	4450078; RRID: AB_3082977
Anti-ASCL1 (clone 24B72D11.1)	BD Biosciences	556604; RRID: AB_396479
Anti-OLIG1 (clone 257219)	R&D Systems	MAB2417; RRID: AB_2157534
Anti-MPO (clone E1E7I)	Akoya	4250083; RRID: AB_2927678
Anti-FOSL1 (clone D-3)	Santa Cruz Biotechnology	sc-376148, custom carrier-free; RRID: AB_11012022
Anti-NFP (clone RMdo-20)	Invitrogen	13–1300
Anti-SOX2 (clone SP76)	Akoya	4250075; RRID: AB_3094504
Chemicals, peptides, and recombinant proteins		
Panobinostat	Selleckchem	S1030
AZD4547	Selleckchem	S2673
Temozolomide	Selleckchem	S1237
Belnacasan	Selleckchem	S2228
Navitoclax	Selleckchem	S1001
Venetoclax	Selleckchem	S8048
J-104129	R&D Systems	2507
Darifenacin	Selleckchem	S3144
Cevimeline	Selleckchem	S6432
Varespladib	Selleckchem	S1110
Retigabine	Selleckchem	S4734
4-Aminopyridine	Selleckchem	S5028
Gabazine	Selleckchem	E1247
CGP52432	Selleckchem	S0303
Entrectinib	Selleckchem	S7998
Trametinib	Selleckchem	S2673
L-741,626	Cayman Chemicals	22354
Quinpirole	Sigma-Aldrich	Q102
Ruxolitinib	Selleckchem	S1378
Danusertib	Selleckchem	S1107
1-Naphthyl PP1 Hydrochloride	Selleckchem	S7060
SB366791	Selleckchem	S8238
Verbascoside	Cayman Chemicals	24965
Y-27632	Selleckchem	S1049
Optimal Cutting Temperature (OCT) Compound	Sakura Finetek	Cat# 4583
Nuclei Extraction Buffer components (1X PBS, 20 mM Tris-HCl, 320 mM sucrose, 5 mM $CaCl_2$, 3 mM $MgAc_2$, 0.1 mM EDTA, 0.1% Triton X-100)	Sigma-Aldrich	Custom formulation
Bovine Serum Albumin (BSA)	Sigma-Aldrich	Cat# A9647
RNAse Inhibitor	New England Biolabs	Cat# M0314
Paraformaldehyde (16% aqueous solution)	Electron Microscopy Sciences	Cat# 15710
Methanol (ice-cold)	Fisher Scientific	Cat# A456
Phosphate-Buffered Saline (PBS, 1×)	Gibco	Cat# 10010023
Sucrose (≥99.5%)	Sigma-Aldrich	Cat# S7903
Calcium Chloride ($CaCl_2$)	Sigma-Aldrich	Cat# C5670
Magnesium Acetate ($MgAc_2$)	Sigma-Aldrich	Cat# M5661
Ethylenediaminetetraacetic Acid (EDTA)	Sigma-Aldrich	Cat# E9884

(*Continued on next page*)

Continued

REAGENT or RESOURCE	SOURCE	IDENTIFIER
Triton X-100	Sigma-Aldrich	Cat# T8787
Tween 20	Sigma-Aldrich	Cat# P1379
TE Buffer (pH 8.0)	Thermo Fisher Scientific	Cat# BP24731
DAPI	Thermo Fisher Scientific	Cat# D1306
Critical commercial instruments, consumables, kits and assays		
Quick-DNA Microprep Plus Kit	Zymo Research	Cat# D4074
Illumina DNA Prep (M) Tagmentation Kit	Illumina	Cat# 20018705
Nextera DNA CD Indexes Kit	Illumina	Cat# 20018707
High Sensitivity DNA Kit	Agilent Technologies	Cat# 5067-4626
High Sensitivity Protein Kit	Agilent Technologies	Cat# 5067-1580
KAPA Library Quantification Kit	KAPA Biosystems	Cat# KK4835
NovaSeq 6000 Sequencing System	Illumina	N/A
Chromium Controller	10x Genomics	N/A
Chromium Single Cell 3′ Reagent Kit v3/v3.1	10x Genomics	Cat# PN-1000075/PN-1000121
Chromium Next GEM Single Cell ATAC Reagent Kit v1.1	10x Genomics	Cat# PN-1000175
Chromium Next GEM Single Cell Multiome ATAC + GEX Kit	10x Genomics	Cat# PN-1000283
Chromium Single Cell B Chip Kit	10x Genomics	Cat# PN-1000073
PhenoCycler-Fusion Instrument	Akoya Biosciences	Cat# AB-000011
PhenoCycler-Fusion Sample Kit	Akoya Biosciences	Cat# 7000017
PhenoCycler Antibody Conjugation Kit	Akoya Biosciences	Cat# 7000009
Xenium Slides & Sample Prep Reagents	10x Genomics	Cat# 1000460
Xenium Cassette Kit	10x Genomics	Cat# 1000566
Xenium Decoding Consumables	10x Genomics	Cat# 1000487
Xenium Decoding Reagents	10x Genomics	Cat# 1000461
Xenium Cell Segmentation Detection Reagents	10x Genomics	Cat# 1000639
Xenium Analyzer Instrument	10x Genomics	N/A
Falcon Cell Strainer (40 μm)	Corning	Cat# 352340
Dounce homogenizer (2 mL)	MilliporeSigma	Cat# D8938
MWCO Centrifugal Filters, 50 kDa	Millipore	Cat# UFC505096
Agilent 2100 Bioanalyzer Instrument	Agilent Technologies	Cat# 5067-4626
Precision X-RAD 320 Irradiator	Precision X-ray	N/A
Ultra-Low Attachment 384-Well Plates	S-Bio	Cat# MS-9384UZ
Incucyte Live-Cell Imaging System	Sartorius	N/A
Chromium Next GEM Single Cell 3′ GEM, Library & Gel Bead Kit v3.1 (16 rxns)	10x Genomics	PN-1000121
Chromium Next GEM Chip G Single Cell Kit (48 rxns)	10x Genomics	PN-1000120
Dual Index Kit TT Set A (96 rxns)	10x Genomics	PN-1000215
10x Vortex Adapter	10x Genomics	330002
10x Magnetic Separator	10x Genomics	230003
Chromium Next GEM Secondary Holder	10x Genomics	3000332

(*Continued on next page*)

Continued

REAGENT or RESOURCE	SOURCE	IDENTIFIER
Deposited data		
Primary patient sequencing and spatial data	This paper	Database of Genotypes and Phenotypes (dbGaP): phs002371
Human Tumor Atlas Network (HTAN) data portal	This paper	https://humantumoratlas.org/publications/hta4_2024_biorxiv_jonathan-h-sussman
Bulk RNA sequencing of *in vitro* radiation experiment	This paper	NCBI GEO: GSE292623
CELLxGENE interactive data explorer	This paper	https://cellxgene.cziscience.com/collections/9ceda3d2-a55e-4b82-a91a-0190d947459a
Software and algorithms		
Seurat v4 (snRNA/ATAC-Seq) Seurat v5 (CODEX)	https://satijalab.org/seurat/	Hao and Hao et al.[78] Hao et al.[79]
Cell Ranger (snRNA-Seq and snATAC-Seq processing) v3.1.0	https://www.10xgenomics.com/support/software/cell-ranger/latest/analysis/inputs/cr-inputs-overview	10x Genomics
PhenoCycler Experimental Designer v1.0.8	https://www.akoyabio.com/phenocycler	Akoya Biosciences
Signac v1.14.0	https://github.com/stuart-lab/signac	Stuart et al.[80]
SCTransform (R package) v2	https://satijalab.org/seurat/	Included with Seurat
DoubletFinder v3	https://github.com/chris-mcginnis-ucsf/DoubletFinder	McGinnis et al.[81]
InferCNV	https://hub.docker.com/r/trinityctat/infercnv	Tirosh et al.[82]
Monocle 3	https://github.com/cole-trapnell-lab/monocle3	Trapnell et al.[83]
Velocyto v0.17	https://github.com/velocyto-team/velocyto.py	La Manno et al.[84]
Scanpy v1.9.3	https://scanpy.readthedocs.io/en/stable/	Wolf et al.[85]
Mesmer 0.12.1	https://github.com/vanvalenlab/deepcell-tf/blob/master/notebooks/applications/Mesmer-Application.ipynb	Greenwald et al.[86]
ScVelo v0.3.2	https://scvelo.readthedocs.io/en/stable/	Bergen et al.[87]
HdWGCNA v0.2.1	https://github.com/smorabit/hdWGCNA	Morabito et al.[88]
chromVAR	https://github.com/GreenleafLab/chromVAR	Schep et al.[38]
scATAC-pro v1.4.4	https://github.com/wbaopaul/scATAC-pro	Yu et al.[89]
MACS2 (Peak Calling) v2.2.7	https://github.com/macs3-project/MACS	Zhang et al.[90]
ClusterProfiler (R package) v4.10.0	https://github.com/YuLab-SMU/clusterProfiler	Yu et al.[91]
Limma-Voom v3.46.0	https://bioconductor.org/packages/release/bioc/html/limma.html	Law et al.[92]
dream (VariancePartition R package) v0.4.2	http://github.com/GabrielHoffman/variancePartition	Hoffman et al.[93]
fgsea	https://bioconductor.org/packages/release/bioc/html/fgsea.html	Korotkevich[94]
ClevRvis v0.99.6	https://www.bioconductor.org/packages/release/bioc/html/clevRvis.html	Sandmann et al.[95]
Clonalscope v1.0.0	https://github.com/seasoncloud/Clonalscope	Wu et al.[60]
SCENIC/pySCENIC v0.12.1	https://github.com/aertslab/pySCENIC	Aibar et al.[96]

(*Continued on next page*)

Continued

REAGENT or RESOURCE	SOURCE	IDENTIFIER
SCopeLoomR	https://github.com/aertslab/SCopeLoomR	N/A
CIBERSORTx	https://cibersortx.stanford.edu/	Newman et al.[97]
imcRtools (for CODEX spatial analysis)		Windhager et al.[98]
Napari v0.4.14	https://napari.org/stable/	N/A
QuPath v0.4.3	https://qupath.readthedocs.io/en/0.5/	Bankhead et al.[99]
HDBSCAN		McInnes et al.[100]
Spatstat	https://spatstat.org/	N/A
LIANA	https://github.com/saezlab/liana-py	Dimitrov et al.[41]
CellChat v1	https://github.com/sqjin/CellChat	Jin et al.[52]
GraphPad Prism 10	https://www.graphpad.com/	N/A

EXPERIMENTAL MODEL AND STUDY PARTICIPANT DETAILS

Human biospecimens

Primary samples were obtained from patients with high-grade glioma banked at the Children's Hospital of Philadelphia (CHOP) through the Children's Brain Tumor Network (CBTN). All samples were collected prospectively in accordance with the guidelines from the Human Tumor Atlas Network (HTAN). The patient selection was built based on specimen availability. Biospecimens were obtained with parent informed consent according to the Declaration of Helsinki and under the approval of the Children's Hospital of Philadelphia Institutional Review Board (IRB 09–007316). All patient data is deidentified and written informed consent was obtained to publish the indirect identifiers in the present manuscript. All patients underwent an initial tumor resection after histopathological diagnosis of high-grade glioma at the age of 18 years or younger before receiving treatment, followed by a secondary surgical resection or sample acquisition at autopsy. Autopsies aimed to minimize ischemic time to the greatest extent possible with most specimens preserved within several hours with maximum of one day. Germline DNA from either blood or skin samples were acquired from the Children's Brain Tumor Network (CBTN) at CHOP. Patient sample information and relevant clinical metadata are provided in Tables S1 and S2.

Cell lines

Pediatric high-grade glioma cell lines 7316–913, 7316–195, 7316–1763, 7316–1769, 7316–3058 (all spheroid culture), and 7316–1746 (adherent culture) were obtained through the Children's Brain Tumor Network (CBTN) and underwent histopathologic, molecular, and genomic characterization as previously described.[101] Authentication of the cell lines was performed by the CBTN biobank via genomic characterization. All cell lines were evaluated for mycoplasma contamination on a yearly basis and confirmed to be negative. Glioma cells were stably transduced with a lentiviral nuclear red or green fluorescent protein under the EF1a promoter (Sartorius, cat. 4476, Göttingen, Germany) for visualization in live imaging assays. Spheroid cultures were maintained in DMEM/F-12 medium supplemented with 1% glutaMAX (Gibco, cat. 35050061), 100 U/mL penicillin-streptomycin (cat. 15140122), 1X B-27 supplement minus vitamin A (Gibco, Cat. 12587010), 1X *N*-2 supplement (Gibco, cat. 1752001), 2.5 ng/mL human epidermal growth factor (PeproTech, cat. AF-100-15-B), 2.5 ng/mL human basic fibroblast growth factor (PeproTech, cat. 100-18B), and 0.5μg/mL heparin (StemCell, cat. 07980).

METHOD DETAILS

Whole genome sequencing (WGS)

The Quick-DNA Microprep Plus Kit (Zymo Research, D4074) was used to extract genomic DNA (gDNA) from nuclei isolated from human pediatric high-grade glioma (pHGG) tissue samples as per the manufacturer's instructions. Sequencing libraries were generated from 1 to 100 ng of gDNA using the Illumina DNA Prep, (M) Tagmentation kit (Illumina, 20018705) according to manufacturer's instructions. Bead-linked transposomes in tagmentation buffer were added to each sample at 55°C for 15 min in a thermal cycler to tagment gDNA and add adapter sequences. After completion of the reaction, Tagmentation Stop Buffer was added to stop the tagmentation reaction. Post-tagmentation cleanup was then performed to remove tagmented and adapter-tagged DNA from beads. This step was followed by the addition of i7 and i5 index adapters to amplify tagmented DNA. The number of PCR cycles was chosen according to directions in the user guide. The i7 and i5 indices were provided in the Nextera DNA CD Indexes kit (Illumina, 20018707). Amplified libraries were then purified using a double-sided bead purification method as outlined in the user guide. The average fragment size of purified libraries was confirmed using the Agilent 2100 Bioanalyzer with the High Sensitivity DNA kit (Agilent Technologies, 5067–4626) and library concentrations were measured using the KAPA library quantification kit (KAPA, KK4835). DNA libraries were pooled and sequenced on an Illumina NovaSeq 6000 using 150 × 150 bp paired-end reads.

Whole genome sequencing (WGS) analysis

WGS data processing and analysis was performed using published Gabriella Miller Kids First Data Resource Center (KFDRC) workflows using their corresponding public applications as implemented on the Cavatica - Seven Bridges Genomics cloud computing platform. Sequence alignment was performed using the KFDRC Alignment and GATK HaplotypeCaller application (Revision 0). Genotyping was performed using the Single Sample Genotyping Workflow application (Revision 0). Somatic mutation and structural variant calling for tumors with corresponding normal samples was performed using the KFDRC Somatic Variant Workflow application (Revision 0). Somatic mutation and structural variant calling for tumors without corresponding normal samples was performed using the KFDRC Tumor Only Pipeline (https://github.com/kids-first/kf-tumor-workflow, v0.1.1-beta), which incorporated a custom panel of normal samples (PON) to filter common technical artifacts. This PON file was built using the 10 germline WGS samples that were sequenced as part of this study and generated using a dockerized implementation of GATK (https://hub.docker.com/r/broadinstitute/gatk, version tag 4.1.1.0). This includes the orthogonal mutational calling methods Manta[102] and Mutect2[103] for all samples and Strelka2[104] when paired normal data were available. Manta also provides somatic structural variant calls. Mutation calls from all methods are available at the HTAN data portal (see data availability statement). As mutation effect annotations were missing in the published KFDRC Tumor Only Pipeline for unpaired samples, we generated these annotations after running the unpaired sample pipeline using a Dockerized version of the Ensemble Variant Effect Predictor (Ensembl-VEP, release 93.5). The full repository of KFDRC workflows may be found here: https://github.com/kids-first/. To identify key mutations, we screened all somatic mutations (using the Mutect2 mutation calls) across the COSMIC Cancer Mutation Census database (v100), which provides curated annotations on the roles of specific genes and mutations in oncogenesis across cancer types.[105]

Methylation profiling and classification

Genomic DNA was extracted as described above for WGS. The Illumina EPICv2 methylation array was used for profiling through the CHOP Center for Applied Genomics core. Tumor classification was performed using online implementation of the Heidelberg Epignostix CNS Tumor Classifier (v12.8)[106] (https://app.epignostix.com/) and the Bethesda V2 CNS classifier (https://methylscape.ccr.cancer.gov/). Methylation profiling was conducted for all samples at the initial timepoint and was conducted for post-therapy samples in cases where there was low classification confidence in the diagnostic samples.

Tissue and sample preparation for single-nucleus RNA and ATAC sequencing

Fresh frozen tumor samples were embedded in optimal cutting temperature (OCT) compound and cryosectioned into 40 μm tissue scrolls. Cryosections (4–6 scrolls) were homogenized by using a 2-mL Dounce homogenizer (MilliporeSigma, D8938) with 1 mL ice-cold Nuclei Extraction Buffer (NEB, consisting of 1X PBS, 20mM Tris-HCl, 320mM sucrose, 5mM CaCl2, 3mM MgAc2, 0.1mM EDTA, and 0.1% TrionX-100). The tissue was homogenized 10 times with pestle A and 10–12 times with pestle B on ice. After ensuring that the tissue had been dissociated completely, an additional 500 μL of NEB buffer was added into each sample, then transferred from the homogenizer to a 1.7 mL Eppendorf tube with filtration using a 40 μm cell Strainer (Falcon, 352340). Filtered samples were incubated on ice for 5 min. Nuclei were centrifuged at 500-600g for 7 min at 4°C and the pellet was washed twice with 1 mL of ice-cold Wash Buffer (1X PBS, 1% BSA, and 0.2U/μL RNAse inhibitor). The washed nuclei pellet was resuspended in an appropriate volume of resuspension buffer (1X PBS and 0.04% BSA), filtered through a 40 μm cell Strainer (Falcon, 352340) and nuclei were manually counted using a hemocytometer before proceeding to library preparation. In cases where multiple regions were profiled (for snRNA-Seq only), scrolls from opposite sides of the tumor block were sectioned.

Single-nucleus RNA sequencing (snRNA-Seq)

Single nuclei suspensions immediately underwent library preparation using the Chromium Single Cell 3′ Reagent Kit v3 or V3.1 (10x Genomics) according to the manufacturer's instructions. Library quality was assessed using the Bioanalyzer Agilent 2100 with the High Sensitivity DNA chip (Agilent Technologies, 5067–4626). Indexed libraries were pooled and sequenced on an Illumina NovaSeq 6000 using sequencing parameters 28:8:0:87 (read1:i5:i7:read2, bp) with an average sequencing depth of 50,000 read pairs per nucleus.

Single-nucleus assay for transposase-accessible chromatin using sequencing (snATAC-Seq)

Single nuclei suspensions immediately underwent library preparation with the Chromium Next GEM Single Cell ATAC Reagent kit V1.1 (10x Genomics) as per manufacturer's user manual. Library quality was assessed using the Bioanalyzer Agilent 2100 with a High Sensitivity DNA chip (Agilent Technologies, 5067–4626). Indexed libraries were pooled and sequenced on an Illumina NovaSeq 6000 using sequencing parameters 49:8:16:49 (read1:i5:i7:read2, bp) with an average sequencing depth of 50,000 read pairs per nucleus.

Sample preparation and sequencing of RNA+ATAC multiomic sequencing

Nuclei were isolated using the same protocols as for snRNA/snATAC-Seq. Single-nuclei suspensions were immediately processed using the 10X Chromium Next GEM Single Cell Multiome ATAC + Gene Expression (GEX) Reagent Kits (see User Guide_RevF provided by the manufacturer). Libraries were sequenced on a NovaSeq 6000 using sequencing parameters 28:10:10:90 format for GEX libraries and 50:8:24:49 for ATAC libraries (read1:i5:i7:read2, bp).

Processing and quality control filtering of snRNA-Seq data

Read count matrices for snRNA-Seq data were generated from raw FASTQ files using Cell Ranger v3.1.0. Reads were aligned to the GENCODE Release 34 (GRCh38.p13) transcriptome reference. The resulting count matrices were processed and analyzed using Seurat v4.[78] Quality control filtering was applied to each cell, using filters of 500 < nFeature_RNA <8000 and mitochondrial read percentage <10%. Poor quality samples containing fewer than 500 cells passing quality control thresholds were excluded from downstream analysis. For two samples of borderline but passable quality (7316–7545, and 7316–7559) we instead used filters of 300 < nFeature_RNA <8000 and mitochondrial read percentage <20% for atlas construction, to ensure sufficient representation of these critical longitudinal post-therapy specimens. Notably, cells falling between the 10–20% mitochondrial threshold comprised a negligible fraction (1.1%) of the total dataset. Doublets were called and removed using the DoubletFinder package (v3)[81] using a doublet proportion estimate of 7.5% and other parameters as default. For all paired boxplot comparisons across time points, the more stringent filters (10% mitochondrial read percentage, nFeature >500) were applied before computing the proportions and respective statistics to ensure consistent comparisons. In cases where multiple regions were profiled for one tumor specimen (for snRNA-Seq only), datasets were merged and treated as a single sample for all downstream analysis unless otherwise specified.

Sample integration, clustering, and cell type annotation of snRNA-Seq data

Initial snRNA-Seq data processing was performed using the Seurat v4 package. Due to computational constraints, data were randomly downsampled so as not to exceed 200,000 total cells, preferentially downsampling cells from samples with a higher cell count to preserve cells in samples with lower cell counts. Cell cycle scores were computed using the *CellCycleScoring* method with annotated cell cycle genes (2019 update). Integration was performed by reciprocal principal component analysis (RPCA) at a patient level. In detail, each patient was normalized by *SCTransform* (v2) with regression of mitochondrial percentage, S score, and G2M score by Gamma-Poisson generalized linear model. A total of 3,000 features were chosen by *SelectIntegrationFeatures* followed by PCA. The *FindIntegrationAnchors* function was run using top 30 PCs. Following integration, PCA was repeated on integrated features with *RunUMAP* and *FindNeighbors* computed using the top 30 PCs. Louvain clustering was performed by *FindClusters* at a resolution of 0.6. Differentially expressed genes for each cluster were calculated using the *FindAllMarkers* function with *assay* = "RNA" and *test.use* = "wilcox." Cluster annotation was performed by manual review of differentially expressed genes and canonical cell type-defining genes, allowing for identification of normal cell type populations including immune and stromal cells as well as a heterogeneous and admixed population of other neuronal and glial cells whose neoplastic versus normal status was inferred by downstream copy number alteration analysis. The remaining cells were added to the dataset as follows. These cells were first normalized with *SCTransform* and integrated through projection with Seurat v5[79] using *FindTransferAnchors* with *dims* = 1:50, followed by *MapQuery* using the integrated PCA and integrated assay with default parameters.

Inference of neoplastic versus normal cells by copy number alteration analysis

Neoplastic versus normal cell annotation was inferred by the presence or absence, respectively, of copy number alterations (CNA) detected from snRNA-Seq data using a dockerized implementation of InferCNV[82] (https://hub.docker.com/r/trinityctat/infercnv, version tag 1.11.1). Due to computational constraints, the downsampled dataset as described above was used for all analysis of neoplastic cells in the snRNA-Seq data. Input parameters included *cutoff* = 0.1 (recommended for 10x Genomics snRNA-Seq data), as well as *cluster_by_groups* = FALSE and *analysis_mode* = "subclusters" in order to cluster cells by distinct copy number profiles. All samples for a given patient, including all time points, were run together in order to capture CNA clusters that may be shared between different tumor regions or time points. Unambiguous normal cell clusters identified during the Seurat integrated analysis of snRNA-Seq data were aggregated into three separate normal cell categories (specifically, mature neurons and oligodendrocytes, white blood cells, and vascular cells) which were then used as normal reference populations for inferCNV. The remaining non-reference cells (comprising the "other neuronal + glial" cluster) were passed through the inferCNV pipeline. The inferCNV method clusters cells based on their CNV profiles, yielding 5–8 distinct subclusters per patient. The inferCNV-derived clusters are distinct from the Louvain-derived clustering utilized elsewhere in the analyses. CNVs are then called for each of these clusters using a Hidden Markov Model (HMM). However, this step is prone to false positive results and spurious CNV calls. Therefore, we manually inspected the CNV calls for each subcluster, compared them to the WGS CNV track, and manually assigned a label of tumor or normal, which enables the precise identification of neoplastic cell subclusters while excluding spurious CNV calls. If the cluster exhibited CNAs that matched those found in the WGS data, it was annotated as neoplastic otherwise it was annotated as non-neoplastic. Given that the WGS data represents a mixture of multiple subclones, if any of the inferCNV-based alterations aligned with a CNV in the WGS data, we annotated the cells as malignant cells. Conversely, if none of the inferCNV-based alterations aligned with any apparent CNV in the WGS data, then we annotated the inferCNV-cluster as normal cells. Each patient was analyzed separately through this process and independently of other patients, and thus the results were not influenced by the overall composition of the cohort.

snRNA-seq malignant cell state analysis

To further dissect the heterogeneity of the malignant cells, the large cluster of "other neuronal and glial" cells were extracted and re-integrated using Seurat v3[1] reciprocal PCA integration. We first subsetted the neuroglia cells that were predicted to be malignant by CNV analysis from the downsampled Seurat object and split the object by sample ID using the *SplitObject* function. Each sample was processed individually using the standard Seurat pipeline, and then we selected 2,000 variable features with the

SelectIntegrationFeatures function followed by running *FindIntegrationAnchors* function with *reduction* = "rpca" and *dims* = 1:30 followed by the *IntegrateData* function with *k.weight* = 50 and *dims* = 1:30. We then ran the *ScaleData*, *RunPCA and FindNeighbors* with default parameters and *FindClusters* functions with *resolution* = 0.3 and *RunUMAP* with dims = 1:30 on the *integrated* assay. To annotate each cluster of the malignant cells, we calculated the signature scores of canonical cell states defined by Neftel et al.[11] as well as cell cycle S and G2M phase scores using the *AddModuleScore* function in Seurat. Differentially expressed genes (DEGs) between each cluster and within each cluster across time points were calculated using the *FindAllMarkers* function with *assay* = "RNA", *logfc.threshold* = 0.1, *min.cells.features* = 20, *max.cells.per.ident* = 500, *test.use* = "wilcox." A pathway analysis was conducted using the *enrichR* function in the ClusterProfiler[91] R package, with the input of differentially expressed genes for each cluster defined by the average log2 fold change in expression >0.5 and restricted to genes expressed in a higher proportion of cells in the respective cluster than in all other clusters (i.e., *pct.1* > *pct.2*). The pathway databases used were: *GO_Biological_Process_2023* (from Gene Ontology), *KEGG_2021_Human, Reactome_2022,* and *MSigDB_Hallmark_2020* (from the Molecular Signatures Database). Each cluster was then manually annotated based on these signature scores, DEGs and pathways.

Differentiation trajectory analysis of malignant cells

Cell state trajectory was inferred through three orthogonal methods: reference mapping, velocity, and pseudotemporal ordering. Reference mapping was conducted through projection of the neoplastic cells to an atlas of the fetal brain (Couturier et al.).[13] Briefly, the reference dataset was filtered for annotated cells with 1,500 < nCount_RNA <20,000 and mitochondrial percentage less than 20%, then reprocessed with Seurat v4 using *SCTransform* with the top 5,000 variable features and a PCA was computed. The neoplastic cells were then re-normalized using *SCTransform* for each patient and projected using the *FindTransferAnchors* function with *dims* = 1:50 followed by the *MapQuery* function with default parameters.

For velocity analysis, velocyto (v0.17)[84] was used to generate feature/barcode matrices of unspliced gene expression data using the output from the Cellranger as input for each of the snRNA-Seq datasets. Next, scanpy (v1.9.3)[85] and scVelo (v0.3.2)[87] were used to combine the spliced and unspliced feature barcode matrices. The data was processed using the *filter_and_normalize* function and moments were computed using the *moments* function with default parameters. RNA velocity was then identified using the stochastic mode from scVelo. Pseudotemporal ordering was conducted using Monocle3[107] using the *learn_graph* and *order_cells* functions with default parameters. The GPC-like cell state was selected as the root node.

Reference mapping of published datasets on pHGG neoplastic cell atlas

Published snRNA-Seq data was obtained for H3G34R/V glioma,[21] H3K27M-altered glioma and H3-wildtype pHGG.[15] Malignant cells were subset based on published annotations. Datasets were split by patient and projected individually using the Seurat v4 workflow. Data for each patient was log-normalized, 2000 variable features were selected and scaled, and a PCA was computed. The data were then projected onto neoplastic pHGG atlas using the *integrated* assay with the *FindTransferAnchors* function followed by the *MapQuery* function with the top 50 dimensions. The neoplastic cell state annotation was transferred to the query datasets and the projected data was visualized on the pHGG neoplastic cell atlas UMAP. The projection confidence scores indicate the extent of similarity to the projected cell state.

Cohort-level analysis of pre-versus post-treatment gene expression changes

Method 1 (GLMM): In order to test for significant pre-treatment versus post-treatment gene expression changes assessed in snRNA-Seq data at a patient cohort level, we applied a generalized linear mixed model (GLMM) framework based on Limma-Voom (v3.46.0)[92] and Differential expression for repeated measures (dream package, v0.4.2).[93] Notably, the extended Limma-Voom framework has built-in support for random effects modeling, which was used here to avoid pseudoreplication when patients had multiple samples from the same timepoint. Two separate GLMM analyses were performed in a pseudobulk manner based upon snRNA-Seq count matrices computed on either 1) neoplastic cells inferred by CNA analysis or 2) myeloid cells from each snRNA-Seq sample. Prior to Limma-Voom, samples with fewer than one million total reads in their corresponding pseudobulk count matrices were excluded. A counts per million (CPM) threshold of 10 was used to call genes as expressed or not expressed, and a gene was only kept if it met this threshold in at least 10 samples. Timepoint (diagnostic versus first post-treatment sample) was treated as a fixed effect and patient ID was treated as a random effect. The effect of autopsy versus secondary surgical resection was evaluated as a fixed effect covariate with negligible differences in the results. One patient (C15498) was excluded from analysis after it was revealed during clinical data review that both timepoints were obtained post-radiation therapy due to a prior history of mixed high-grade/low-grade glioma. Genes with FDR <0.05 by the Benjamini-Hochberg method were considered statistically significant. A gene set enrichment analysis (GSEA) was conducted to compare differentially expressed pathways over therapy. All genes from the GLMM analysis were sorted by LogFC to use as input to pre-ranked GSEA using the fgsea package.[94] Pathways were sourced from the Molecular Signatures Database (MsigDB) Hallmark gene sets[108] and the KEGG database.[109] The IDH/H3-WT diffuse glioma subset analysis was conducted analogously using patients: C799746, C34809, C2399853, C176874, C1061121, C2542041, C107625.

Method 2 (Meta-analysis): For each patient, genes were assigned a nominal *p*-value using the *FindMarkers* function in Seurat v4, comparing pre-versus post-treatment expression changes in a pseudobulk manner using only neoplastic cells as inferred by the presence of CNA in both timepoints. The resulting two-sided *p*-values were converted to their corresponding absolute *Z* score

and assigned a sign based on the direction of fold-change in pre-versus post-treatment analysis for each patient. The resulting signed Z-scores for each patient were then combined by Stouffer's *Z* score method of meta-analysis, resulting in a composite signed *Z* score and corresponding two-sided *p*-value. Genes with FDR <0.05 by the Benjamini-Hochberg method were considered statistically significant.

snATAC-seq data processing

snATAC-Seq data for each sample was first demultiplexed using CellRanger-ATAC v.1.1.0 (10x Genomics). The fastq files were then processed using the *process* module of scATAC-pro (v1.4.4)[89] with the default parameters. Briefly, the raw reads were aligned to the hg38 genome assembly. Peaks were called using MACS2.[90] Barcodes with more than 2,000 total fragments, <20% mitochondrial reads, and >25% fraction of reads in peaks (FRiP) were identified as cells. The peak-by-cell count matrix was constructed and used for downstream analyses.

snATAC-seq data integration

To integrate data from all patients, we first merged the peaks from different samples if two peaks are within 500bp of each other by the *mergePeaks* module of scATAC-pro. The peak-by-cell count matrix was then reconstructed based on the merged peaks using the *reConstMtx* module of scATAC-pro. Matrices from all samples were concatenated and loaded into Seurat with an extra *ChromatinAssay* added. The data was processed using Signac[80] as follows: The Seurat object was split by sample ID and each sample was then processed through *FindTopFeatures* (with the minimum cutoff equal to 1% the number of cells present in the subset), *RunTFIDF* and *RunSVD* of Signac. *FindIntegrationAnchors* function was run with parameters *reduction*="rlsi" and *dims* = 2:30 with samples 4036 and 4037 as reference, which were from the patient with the greatest number of immune cells as found in the snRNA-Seq data. The anchor features were defined as peaks that are accessible in more than 3% of cells in at least one of the patients. Then, Signac *IntegrateEmbedding* function was run with default parameters. The cells were further clustered with the *FindNeighbors* and *FindClusters* (with *resolution* = 0.8) functions in Seurat. For visualization, the UMAP was constructed using *RunUMAP* with *reduction* = "integrated_lsi" and *dims* = 2:30.

snATAC-seq cell type annotation

Cells in snATAC-Seq were annotated using the label transfer pipeline of Seurat v3[110] with minor modifications. First, the gene activity score per cell was computed by summarizing fragments overlapping with the gene body or gene promoter (+/− 2kb around the TSS). The ACTIVITY assay was then added to the Seurat object through the *CreateAssayObject* function in Seurat using the gene activity score matrix, followed by log normalization through the *NormalizeData* function. Next, the *FindTransferAnchor* function was run using the downsampled snRNA-Seq Seurat Object as *reference* and the snATAC-Seq Seurat object as *query*, the highly variable genes of snRNA-Seq as *features,* ACTIVITY as the *query.assay,* and *reduction* = "cca." Finally, the *TransferData* function was run with the annotated cell types in snRNA-Seq as *refdata*, *weigth.reduction* = "integrated_lsi", and *dims* = 2:30. The snRNA-Seq "other neuronal and glial" population was further annotated as neoplastic/normal based on the inferCNV results before label transfer. Confident annotations were defined as cells having a maximum prediction score >0.9, and each cluster was assigned to the most abundant confident cell type annotation within that cluster. The predicted labels were further validated through the signature scores calculated based on signatures genes from Couturier et al.[13] data for each type of the cells. The cells which had been assigned to non-neoplastic neuroglial cells were re-assigned as mature neurons based on the signature score (Figure S2B).

snATAC-seq malignant cell state analysis

To further dissect malignant cells in snATAC-Seq data, we extracted the large cluster of neural and glial cells and re-integrated them by Signac pipeline, using the same process used to integrate the complete samples but without the selection of reference samples. Malignant cells were identified via label transfer as described above and were clustered using the *FindClusters* (*resolution* = 0.75). Two clusters were identified that captured low quality cells and were excluded followed by re-integration of the data. Then, we performed label transfer by Seurat as described above, using the cell state annotation of malignant cells in snRNA-Seq data as the reference. Cells with label transfer prediction score >0.4 were maintained for subsequent analysis (Figure S1).

Transcription factor motif analysis

Transcription factor (TF) motif enrichment scores was computed using chromVAR[38] for each cell. The cisBP core TFs "human_pwms_v2" from the chromVARmotif R package were used as the TF motif database. TF motifs enriched in each snATAC-Seq cell cluster were identified by performing a one-sided Wilcoxon rank-sum test comparing chromVAR deviation score between the cluster and other clusters after downsampling each comparison group to 500 cells each.

Construction of transcriptional regulatory network

The transcriptional regulatory network for each neoplastic cell state was constructed as previously described[111] with minor modifications. We first co-embedded the snATAC-Seq and snRNA-Seq data per sample using the standard Seurat pipeline. Then we identified metacells using hdWGCNA[88] with parameters *k* = 20, *max_shared* = 5, *min_cells* = 50, *reduction* = "pca" and *ident.group* = "seurat_clusters." Metacells containing between 4 and 16 snRNA-Seq cells were kept for further analysis. The gene-by-metacell

expression matrix and the peak-by-metacell accessibility matrix were calculated as the average normalized expression and normalized accessibility of all cells within the metacell, respectively. Metacells from different samples were then combined and the Enhancer-Promoter (EP) interactions were predicted using a linear regression model for each gene on metacells, with the gene expression in each metacell as the dependent variable, and the accessibility of the peaks within ±500kb of the gene promoter as the independent variables. Significant EP interactions were defined based on a peak regression coefficient >0.1 and Benjamini-Hochberg-adjusted *p*-value <0.05. Predicted TF-target genes pairs were defined if the TF motif was present at the enhancer of a predicted EP interaction and both the TF and target gene were expressed in at least 20% of the cells within a given cell state.

Multiomic sequencing data analysis

Multiomic RNA+ATAC sequencing was performed on three samples (2 existing samples and 1 additional sample) to evaluate the accuracy of malignant cell state annotation in the snATAC-Seq data. Multiome data was first demultiplexed using CellRanger-Arc v2.0.2 (10x Genomics), then processed using the *count* function with default parameters, and aligned to the GRCh38-20202-A-2.0.0 reference. Analysis was conducted using Seurat v5.1.0[79] and Signac v1.14.0.[80] Samples were filtered for RNA mitochondrial UMI percent <10%, nFeature_RNA between 500–10,000, nCount_ATAC between 2,000–100,000, and ATAC transcription start site (TSS) enrichment >2. Doublets were called and removed using the DoubletFinder package[81] using a doublet proportion estimate of 7.5%, SCTransform normalization, and the top 30 dimensions. ATAC regions were quantified based on the integrated peak set constructed in the snATAC-Seq analysis. Coarse cell types were annotated through projection to our reference snRNA-Seq dataset. Briefly, multiome data was merged, normalized with SCTransform, and then projected to the integrated dataset using the *FindTransferAnchors* and *MapQuery* functions with the top 50 dimensions. Malignant cell types were called using InferCNV[82] as before with minor modifications. InferCNV v1.20.0 was run with parameters *cutoff* = 0.1, *cluster_by_groups* = FALSE, *analysis_mode* = ''subclusters'', *denoise* = TRUE, *HMM* = TRUE, *leiden_resolution* = 0.005. Cells annotated as oligodendrocytes/neurons, vascular cells, and white blood cells were used as the normal reference, and all multiome cells were analyzed together. Cells with clear CNV patterns (comprising most of the other neuronal/glial population) were carried forward as putative neoplastic cells. These cells were merged with the snRNA-Seq data, and the full dataset was reintegrated using RPCA integration (split by sample ID) and clustered at a resolution of 0.75 using the same protocols as for the snRNA-Seq data. Clusters aligned directly to those found in snRNA-Seq dataset and were manually annotated. This full integration yielded a more accurate annotation than a one-directional projection. The corresponding multiome ATAC component was then analyzed using chromVAR[38] to assess transcription factor motif accessibility given the ground-truth transcriptomic cell states using the same procedures as for the snATAC-Seq dataset.

Cell-cell communication analysis

To assess ligand-receptor interactions between cell populations in the tumor microenvironment, we implemented the Ligand-Receptor Analysis Framework (LIANA) v0.1.12,[41] which infers cell-cell communication using a consensus of 16 cell signaling database resources and 5 CCC methods (Natmi,[112] Connectome,[113] LogFC Mean, SingleCellSignalR,[114] CellphoneDB[115]) with default parameters. The neoplastic cell states and myeloid subpopulations as annotated above along with the remaining non-neoplastic populations were included. We considered the consensus rank generated via Roust Rank Aggregation as the significance *p* value to predict the intercellular crosstalk between each pair based on the expression level of known receptors and ligands in the respective clusters and filtered interactions to those with *p*-value <0.05. The number of significant interactions between cell populations was quantified, and the most relevant interactions were manually selected to plot. CellChat was used in parallel using the CellChatDB database.[52] The significant cell-cell interactions were determined using CellChat default parameters, with population size accounted for and ''trimean'' used for calculating mean gene expression.

Myeloid subtype analysis

Tumor-associated myeloid populations were investigated by subsetting the macrophage/microglia population from the full snRNA-Seq dataset and splitting this object by patient ID using the *SplitObject* function. Each sample was processed individually using SCTransform regressing out nCount_RNA, mitochondrial read percentage, and ribosomal read percentage. We then selected 3,000 variable features with the *SelectIntegrationFeatures* function followed by running *FindIntegrationAnchors* function with *reduction* = ''rpca'', *dims* = 1:30, and *k.anchor* = 20 followed by the *IntegrateData* function with *dims* = 1:30. We then ran the *RunPCA, RunUMAP, FindNeighbors,* and *FindClusters* functions on the *integrated* assay with *dims* = 1:30 and *resolution* = 0.1. We then projected this data onto the GBM atlas[116] as described above and observed two clusters that represented misclustering of neuroglial cells, confirmed by specific expression of astrocyte and oligodendrocyte identity genes. These clusters were removed, and the remaining cells were reprocessed and reintegrated with the same procedure as above and reclustered with *resolution* = 0.6. To annotate each cluster of the myeloid cells, we first calculated the signature scores of canonical microglia and bone marrow-derived macrophages defined by Müller et al.[117] as well as cell cycle S and G2M phase scores using the *AddModuleScore* function in Seurat. Differentially expressed genes (DEGs) for each cluster were calculated using the *FindAllMarkers* function with *test.use* = ''wilcox'', *min.pct* = 0.10, *min.diff.pct* = 0.10, *logfc.threshold* = 0.10, and clusters were annotated manually based on these gene signatures and DEGs.

SCENIC transcriptional regulatory network (TRN) analysis of myeloid cells

The Single-Cell Regulatory Network Inference and Clustering (SCENIC) algorithm[96] was used to identify transcription factors regulating myeloid cell states. It was run using the pySCENIC implementation as previously described[118] on the scRNA-seq data, after conversion of the Seurat object to loom format. The GRNBoost2 algorithm was used for GRN inference. To predict transcription factor regulons, we used the human v9 cisTarget motif collection and the hg38_refseq-r80 databases with the 500bpUp100Dw and $TSS^{+/-}$10kb search spaces. All relevant databases were obtained from: https://resources.aertslab.org/cistarget/. The pySCENIC implementation of AUCell was used to score the activity of regulons for each cell. The *SCopeLoomR* package (https://github.com/aertslab/SCopeLoomR) was then used to extract the regulons and AUCell matrix from the resulting loom file, and the final AUC matrix was added to the initial Seurat object for visualization and analysis. Differential regulons were identified using the *FindAllMarkers* function using the Wilcoxon rank-sum test with "*logfc.threshold* = 0.01."

Malignant subclone analysis

To study the evolution of malignant subclones in the patient-matched longitudinal samples, we applied Clonalscope (v1.0.0),[60] which utilizes both snRNA-Seq data and paired WGS data. Clonalscope identifies copy number variation (CNV) segments with a Hidden Markov Model (HMM) from the paired WGS data, and then estimates the fold change of CNV segments at a single cell level using the snRNA-Seq data with a Poisson model. The HMM results in CNV segments of variable length on the order of approximately hundreds of kilobases, yielding a cell-by-CNV segment matrix. Then, it identifies tumor subclones through a Bayesian non-parametric clustering process based on the estimated CNVs. Clonalscope was run with default parameters on 14 of the 16 patients. Patient C70848 was excluded due to having a single time point and patient C1060383 was excluded due to an insufficient amount of non-neoplastic cells for the Clonalscope algorithm. The required normal/reference cells were defined by manual inspection of the inferCNV profiles as described above. Paired WGS data augments identification of CNV segments, improving malignant subclone delineation. WGS data was first analyzed by CNVkit as described above and iteratively refined by (1) merging continuous segments that share the same copy number state (amplification, neutral, or loss) and (2) merging each with neighboring segments if its size is <5% of both neighboring segments and if both neighboring segments share the same copy number state. This process denoises the WGS-defined CNV segments for use with Clonalscope.

Clonalscope was then applied to estimate CNV profiles of single cells at the earliest time point for each patient, through a non-parametric clustering process. The estimated mean CNV profile of each subclone is utilized as a prior to trace similar subclones or discover new subclones from subsequent time points. For each patient, the shifts in malignant subclone proportions were visualized using clevRvis (v0.99.6),[95] with the *fishPlot* function using a spline fit. Clones were defined as having expanded if their percentages increased over time and comprised at least 10% of the malignant population at the latest time point. The average values of estimated CNVs were summarized for each chromosome arm. CNV gain or loss was binarized as follows: average CNV >1.25 was defined as a copy number gain and <0.75 as a copy number loss. For each chromosome arm, a Fisher's exact test was used to assess for recurring copy number alterations comparing the gain or loss of each chromosome segment relative to the gain or loss of all other segments and adjusted using the Benjamini-Hochberg method. Because the HMM-derived CNV segments vary for each patient, we utilized gene-level CNVs to assess the overall copy number similarity of tumor subclones between patients. To assess gene-level CNVs, we first identified the genes within each segment by overlapping the genomic regions with the hg38 human genome. The estimated CNV value for each segment was used as the gene-level CNV for all genes overlapping the respective segment.

To identify pathways enriched in expanded subclones, differentially expressed genes were calculated using the Wilcoxon rank-sum test comparing each subclone to the rest of the malignant cells within each patient. A gene set enrichment analysis was performed via clusterProfiler v4.0.5 with the Gene Ontology, KEGG, Cancer Hallmarks, and Reactome pathways from the Molecular Signatures Database using default parameters.

CODEX staining

CODEX staining was done using the sample kit for PhenoCycler-Fusion (Akoya, 7000017) according to Akoya's PhenoCycler-Fusion user guide with modifications to include a photobleaching step and overnight incubation with antibodies at 4°C. FFPE samples were sectioned at 5 μm thickness and mounted onto charged slides (Leica, 3800080). Sample slides were baked overnight at 60°C and allowed to cool to room temperature. Sample slides were deparaffinized in Xylenes (Sigma, 534056) twice and rehydrated in a graded series of ethanol concentrations (2 times 100%, 90%, 70%, 50%, 30% and 4 times ddH2O). Antigen retrieval was performed in 1x Dako Target Retrieval Solution, pH 9 (Dako, S2367) with a pressure cooker for 20 min. After equilibrating to room temperature, sample slides were washed 2 times with ddH2O and once with 1x PBS before being submerged in a four-well plate containing 4.5% H2O2 and 20mM NaOH in PBS (bleaching solution) for photobleaching. The four-well plate was sandwiched between two broad-spectrum LED light sources for 45 min at 4°C. After 45 min, sample slides were transferred to a new four-well plate with freshly-made bleaching solution and photobleached for another 45 min at 4°C. Sample slides were washed 3 times in PBS and then 2 times in hydration buffer. Sample slides were equilibrated in staining buffer for 30 min and incubated in the antibodies (Table S13) diluted in staining buffer plus N Blocker, G Blocker, J Blocker, and S Blocker overnight at 4°C. After antibody incubation, sample slides were washed 2 times in Staining Buffer and fixed for 10 min in 1.6% paraformaldehyde (Electron Microscopy Sciences, 15710) storage buffer. Sample slides were washed 3 times in PBS and incubated in ice-cold methanol for 5 min. After incubation in methanol, sample slides were

washed 3 times in PBS and incubated in final fixative solution (1000μL of PBS +20 μL of Akoya's final fixation reagent) for 20 min at room temperature. The sample slides were then washed 3 times in PBS and stored in storage buffer prior to imaging.

CODEX antibody conjugation

Akoya antibodies were purchased pre-conjugated to their respective CODEX Barcode (Table S13). All other antibodies were custom conjugated to their respective CODEX barcode (Table S13) according to Akoya's PhenoCycler-Fusion user guide using the antibody conjugation kit (Akoya, 7000009) following manufacturer's protocol. Briefly, 50 μg of carrier-free antibodies were concentrated by centrifugation in 50kDa MWCO filters (EMD Millipore, UFC505096) and incubated in the antibody disulfide reduction master mix for 30 min. Buffer exchange of the antibodies was then performed to stop the reduction reaction by centrifugation, addition of conjugation solution, and an additional centrifugation. Respective CODEX barcodes resuspended in nuclease free water and conjugation solution were added to the concentrated antibody and incubated for 2 h at room temperature. Conjugated antibodies were purified by 3 buffer exchanges with purification solution. Antibody storage buffer (100 μL) was added to collect the concentrated purified antibodies. Successful conjugation was confirmed using the Agilent 2100 Bioanalyzer with the Agilent Protein High Sensitivity kit (Agilent Technologies, 5067–1580), following the manufacturer's instructions.

CODEX imaging

CODEX reporters were prepared according to Akoya's PhenoCycler-Fusion user guide and added to a 96-well plate. The PhenoCycler-Fusion experimental template was set up for a CODEX Run using Akoya's PhenoCycler Experiment Designer software according to Akoya's PhenoCycler-Fusion user guide. Details on the order of fluorescent CODEX Barcodes and microscope exposure times can be found in Table S14. The PhenoCycler-Fusion experimental run was performed using Akoya's Fusion 1.0.8 software according to Akoya's PhenoImager Fusion user guide. Images were taken and pre-processed (stitching, registration, background subtraction) with Akoya's PhenoImager Fusion microscope using default settings. Final images were evaluated, and selected samples were reimaged with adjusted exposure times based on manual review. After imaging, slides were stained with hematoxylin and eosin (H&E) and imaged at 40x resolution. CODEX data were visualized using QuPath v0.4 and Napari v0.4.18.

CODEX data segmentation

Nuclear segmentation with a fixed pixel expansion of 4 pixels (equivalent to 2 μm) was performed using Mesmer[86] for each image to enable the capture of cytoplasmic and membrane markers while limiting lateral spillover. Maxima threshold and interior threshold were each set to 0.3. To generate the necessary input of a two-channel TIFF, we used DAPI for the nuclear channel and a composite channel of GLUT1, CD3e, CD14, and CD68 for the membrane channel although the nuclear segmentation was used. Mean pixel intensity was extracted from each cell segmentation mask, yielding a cell by protein matrix which was carried forward for analysis in Seurat v5.[79] Cells with very low or high raw DAPI expression (<10 or >250 on a UINT8 scale) were removed. Each image was manually cropped to exclude large areas of artifact including tissue folding and detachment, debris, and edge artifact. All marker channels including DAPI, but not blank channels, were retained in the cell by protein matrix of each Seurat object for each sample.

CODEX data integration and annotation

Individual Seurat objects were merged, which was then normalized by CLR normalization in Seurat with *margin* = 2. The Seurat object was again split by sample, and downsampled using the *SketchData* function with *method* = "LeverageScore" with 50,000 cells per sample. The data was scaled, and a principal component analysis was computed. The samples were integrated using the *IntegrateLayers* function with RPCA integration using the first 15 dimensions. The integration features were selected based on manual inspection of each marker across samples to identify markers with consistent staining across the majority of the samples. Cell cycle genes were excluded, and DAPI was included to help identify autofluorescence artifact. The markers selected were: DAPI, CD31, CD44, IBA1, NFP, CD4, ATRX, APOE, CD56, CD163, GFAP, CD11b, S100B, CD206, OLIG1, CD133, SOX2, Vimentin, MPO, HLA-DR, P2RY12, CD8, NeuN, Collagen IV, CD14, CX3CR1, MOG, SPP1, CD3e, CD68, Nestin, CD16, TMEM119, OLIG2, GLUT1.

Cells were clustered using the *FindNeighbors* function on the integrated assay with the top 15 principal components followed by *FindClusters*, and a UMAP was computed for visualization. Based on marker expression, clusters were assigned to an initial annotation of endothelial cells (CD31, Collagen IV), neuroglial cells including tumor cells (SOX2, OLIG2, Vimentin, GFAP, MOG, NFP), myeloid cells (CD68, CD11b, CD14, P2RY12, TMEM119), or T cells (CD3, CD4, CD8). The remaining cells were projected onto this sketched integration using *ProjectIntegration* and *ProjectData* with the same features and dimensions as above. Subsequently, the neuroglia, myeloid, and T cell clusters were subjected to a second round of annotation. They were first subset, downsampled through sketching, scaled, integrated, clustered, and the remaining cells projected using the same parameters as above. Cell type masks were generated for each category and manually evaluated and labeled in Napari v0.4.18. Clusters which were found to represent apparent artifacts including necrotic cells, autofluorescence artifact, tissue folding, paraffin wax drops, and red blood cells were excluded. Blank channels were used to help identify artifacts. $CD4^+$ and $CD8^+$ T cells could not be distinguished via clustering, so manual thresholding based on CD8 was used to distinguish them. All other clusters were labeled based on their marker expression and general morphology. Tumor cell annotations were based on aggregate expression profiles followed by detailed manual inspection of the images for morphology and staining. In DMG samples, tumor cells showed intranuclear H3K27M staining. Non-malignant astrocytes comprised a small fraction of neuroglial cells and could not be effectively separated through expression

profiles. After filtering, cells were subjected to one more round of sketching, integration, and projection in order to build the final UMAP for visualization.

Cellular neighborhood analysis

Neighborhood analysis was performed as previously described[119] using the final cell type annotations, and as implemented by the imcRtools package.[98] Briefly, a k-nearest neighbors graph from all cells was constructed using the *buildSpatialGraph* function in imcRtools with k = 20, which calculates the neighborhood composition of each cell with a sliding window. These windows are clustered using k-means clustering with respect to their proportions of cell types with 15 clusters. Statistical significance of cell type enrichment within each neighborhood was calculated using a hypergeometric test. The *p*-value was calculated based on the following four numbers: (1) the number of cells of a given type in the neighborhood; (2) the total number of cells in the neighborhood; (3) the number of cells of a given type in the CODEX dataset; and (4) the total number of cells in the CODEX dataset. *p*-values were adjusted for multiple hypothesis testing using the Benjamini-Hochberg method and significance was defined as p-adjusted <0.001.

Cell proximity analysis

We measured the proximity of each cell type to every other cell type using the median distance through the spatstat R package.[120] We used the *ppp* and *psp* functions to create point and line segment patterns and quantified spatial proximity using a table of cell type annotations and locations with the *distfun* function. We randomly downsampled the source cell type populations to the larger value between 0.25*number of cells or 50,000 cells and restricted the observation window to a rectangular area bounded by the target cells with the maximum x and y coordinates. The source cell type was skipped if there were fewer than 10 of that cell type in a given sample. We conducted a one-sided permutation test without replacement to determine if the source cell type is significantly close to each target cell type in each sample. We permuted the labels 100 times and calculated their median distance across the 100 permutations. The proportion of distances smaller than that of the cell type is the *p*-value, which was defined as significant if $p < 0.05$.

Identification of timepoint-associated neighborhoods

From the CODEX data, we identified neighborhoods from k-means clustering on windows of 20 cells on each sample independently, rather than all samples aggregated as above. Fifteen neighborhoods were similarly generated for each sample.[119] The neighborhoods in each sample were then split into instances. To generate instances, a 25-nearest neighbors graph was generated from cell spatial coordinates. For each neighborhood, the graph was filtered to its constituent nodes, and each resulting connected component of at least 40 nodes was designated as an instance. We then applied the N-Orbit framework[59] to generate a distance matrix representing all neighborhood instances among the samples. Briefly, for each cell in a neighborhood instance, its cell type identity and the degree of proximity (up to 2) of all possible cell types, was determined by a 6-nearest neighbors spatial graph, denoted an N-Orbit. N-Orbits were represented as vectors with a nucleus (or center cell type) encoding portion and an orbit (or proximity level) encoding portion. Distance between two N-Orbits was the Manhattan distance between their vectors, using a nucleus change penalty of 8. The distance between two neighborhood instances was defined as the minimum collective distance between 500 bootstrapped N-Orbits sampled from each, calculated through cost matrix optimization. Pairwise distances across all neighborhood instances were compiled into an overall distance matrix. Principal component analysis (PCA) was applied to the distance matrix to project neighborhood instances onto the component of highest variance (PC1). Neighborhood instances were traced back to rank their loading contribution to PC1, and the top 10% of neighborhood instances were further inspected for association with timepoint. These neighborhood instances were clustered using HDBSCAN[100] followed by hierarchical subclustering, and clusters were assessed for enrichment for either initial resection or post-therapy using hypergeometric tests. Clusters deemed to be enriched for either were considered timepoint-associated neighborhoods. Lastly, timepoint-associated neighborhood clusters were traced back to their enriched N-Orbits using a bootstrap-permutation test. In each permutation, the nucleus-encoding portion of the N-Orbit was left fixed while the indices of the non-zero values in the orbit encoding portion were permuted, effectively shuffling cell type identities of orbit members while maintaining overall cell type proportions and N-Orbit cardinalities. Occurrences of each N-Orbit in the unpermuted and permuted bootstraps were then compared. The proportion of tests where the N-Orbit was more common in the unpermuted version was recorded as the *p*-value, which was adjusted for multiple hypothesis testing through the Benjamini-Hochberg method.

Xenium tissue slide preparation

Sample preparation for Xenium spatial transcriptomics was done using the Xenium Slides & Sample Prep Reagents (10X Genomics, 1000460). Formalin fixed and paraffin embedded (FFPE) tissue blocks were sectioned into 5 μm sections and placed on Xenium slides within the sample positioning area of 10.45 mm × 22.45 mm. Tissue slides were then baked at 60°C for 2 h in a thermal cycler and deparaffinized for 10 min in xylene twice. Deparaffinization was followed by rehydration in serially decreasing concentrations of ethanol for 3 min in each: twice in 100% ethanol, twice in 96% ethanol and once in 70% ethanol, followed by 20 s in nuclease free water. Tissue slides assembled in Xenium cassette (Xenium Cassette Kit, 1000566, 10X Genomics) were then decrosslinked at 80°C for 30 min and re-equilibrated to 22°C in a thermal cycler to release mRNA for probe hybridization. Custom probes (standalone 300-gene panel) provided as a lyophilized powder were resuspended in TE buffer, pH 8.0 (BP24731, Thermo Fisher Scientific). The resuspended probe solution was vortexed for 5 min and centrifuged briefly at room temperature. The DNA probes were allowed to hybridize to targeted mRNA at 50°C overnight in a thermal cycler. Following hybridization, tissue samples were washed to remove

unbound DNA probes. The hybridized probes were then enzymatically ligated at 37°C for 2 h and amplified at 30°C for 2 h in a thermal cycler. Tissue samples were washed three times in TE buffer for 1 min after amplification. For cell segmentation staining using the Xenium Cell Segmentation Add-on Kit (10X Genomics, 1000662), tissue slides were washed in a series of ethanol concentrations for 2 min in each: 70% ethanol, twice in 100% ethanol and 70% ethanol. Tissue sections were then blocked for 1 h at room temperature and stained with cell segmentation antibodies at 4°C overnight. Following overnight incubation, tissue samples were washed three times in PBS-T (1X PBS and 0.05% Tween 20) for 1 min and incubated in Xenium stain enhancer for 20 min at room temperature. After washing the slides twice in PBS-T for 1 min, slides were incubated in diluted reducing agent B for 10 min. After dehydration in 70% ethanol for 1 min and then twice in 100% ethanol for 1 min, autofluorescence quenching was performed using the Xenium autofluorescence mix in the dark for 10 min at room temperature. Following quenching, tissues samples were washed three times in 100% ethanol for 2 min and dried at 37°C for 5 min in a thermal cycler in the dark. Tissues were then rehydrated in 1X PBS for 1 min followed by PBS-T for 2 min in the dark. Nuclei were counterstained with DAPI and then samples were washed three times with PBS-T in the dark. Sample slides were stored in PBS-T at 4°C in the dark before proceeding to imaging.

Xenium imaging and post-processing

Reagent plates and buffers to be loaded on the Xenium machine were provided in the 10X Genomics kits (Xenium Decoding Consumables, PN-1000487; Xenium Decoding Reagents, PN-1000461; Xenium Cell Segmentation Detection Reagents, PN-1000639) and prepared as per the manufacturer's instructions. After running a successful readiness test on the Xenium analyzer instrument, sample slides in the Xenium cassette without a lid along with reagents and consumables were loaded on the instrument. After successful loading, a sample scan was performed by the instrument to generate a scanned image for review to check autofluorescence and selection of regions of interest (ROIs) on tissue sections. After ROI selection, imaging, decoding, segmentation, and cell assignment was performed by Xenium Onboard Analysis Software v3.0.

Xenium ligand-receptor interaction analysis

A custom 300-gene Xenium panel was manually designed to include tumor and immune marker genes and ligand-receptor genes curated from our snRNA-Seq data and established literature. The Xenium data was manually cropped to yield a region of interest for each sample, and the segmented cell by transcript matrix was loaded into Seurat v5.[79] The data was filtered to include cells with greater than 10 total transcripts (nCount_Xenium) and greater than 5 distinct features (nFeature_Xenium). The data was normalized using log normalization, and the samples were integrated using the *IntegrateLayers* function with RPCA integration using all features and the top 30 dimensions. The data was clustered using Louvain clustering with the top 30 dimensions with *resolution* = 0.3. High confidence tumor and myeloid cell clusters were identified using marker gene expression. A ligand-receptor interaction analysis was performed as previously described.[121,122] Briefly, for each sample we identified all possible pairs of interacting myeloid and tumor cells (defined as cell centroids within 30 μm of each other) using the *buildSpatialGraph* function in the imcRtools R package[98] with *type* = "expansion." Then for each pair, we calculated the product of the log normalized expression of the ligand in the myeloid cell and the receptor in the tumor cell and defined the LR score as the sum of these products across all proximal myeloid-tumor pairs. Ligand-receptor pairs to be tested were curated from the LIANA database.[41] The enrichment significance was determined using empirical shuffling: we randomly selected the same number of non-proximal myeloid-tumor pairs that were separated by greater than 30 μm and calculated the LR score. Then, we generated a null distribution of LR scores by repeating this procedure 1,000 times. A *p*-value was then determined using a one-tailed Z-test and adjusted using the Benjamini-Hochberg method. The fold change was determined as the LR score for the proximal pairs compared to the average of the LR scores for the non-proximal permutations. An aggregate *p*-value was determined using Stouffer's method across samples for each LR pair and then adjusted using the Benjamini-Hochberg method. The aggregate fold change was taken as the average of the fold change values across samples.

Prioritization of drug targets for *in vitro* drug screening

To identify targetable genes for pharmacological manipulation of tumor cell-intrinsic functions, we developed a framework that incorporates transcriptional analysis with drug databases. Drug/target data from two independent drug targets databases (TTD,[123] DrugIDB[124]), as well as a third database (OpenTargets[125]) that focuses on next-generation targets were overlapped with differentially gene expression data from our linear mixed model analysis. Targetable gene products were given a score of +1 if a resulting hit occurred from any of the three databases. To search for drugs that could modify therapeutically induced transcriptional profiles, we inputted top time point-specific DEGs (*n* = 93 upregulated, 74 downregulated) into the LINCS1000[126] database (https://clue.io/query#l1000) under default parameters. This method predicts perturbations that alter the collectively inputted transcriptional profile. Perturbation results across cell lines were filtered for compound-based perturbations with defined targets, false discovery rate (FDR) < 0.25, and effect size (magnitude of normalized connectivity score >0.6). Both initial time point, and post-therapy-specific effects were considered on the basis that upregulated transcriptional profiles may simultaneously include positive effects of therapy in addition to the development of resistance mechanisms and requires experimental study. Thus, any gene targeted through the filtered perturbations was given a score of +1. Next, to predict glioma-specific genes that could mediate cytotoxicity when targeted, we downloaded cell line dependency data from the Cancer Dependency Map (DepMap)[127] portal and searched for genes which showed increased dependency in glioma cell lines (*n* = 83) compared to non-glioma cell lines (*n* = 1070). Genes with negative dependency

scores in glioma cell lines (mean dependency score < −0.1) and dependency mean fold-change >1.5 were assigned +1 to the overall score.

We further prioritized genes based on two methods of differential expression analysis, prioritizing genes that were upregulated post-therapy in order to identify additional single gene dependencies that could be targeted. First, using the linear model analysis, upregulated DEGs were assigned a score as follows accounting for degree of upregulation and statistical significance: logFC >0 and p-adjusted <0.05: +0.5, logFC >0.5 and p-adjusted <0.05: +1, logFC >0.5 and p-adjusted <0.001: +1.5, logFC >1 and p-adjusted <0.05: +1.5 (only the highest score added). Second, a patient-wise meta-analysis approach was used orthogonally, requiring a *Z* score >0 and then assigning a score based on the number of patients in which the gene was upregulated post-therapy: 8–9 patients: +0.5, 10–11 patients: +1, >11 patients, +1.5 (only the highest score added). Lastly, given the significance of the cellular interactions in maintaining glioma proliferation, we added a score of +1 to any genes that were predicted to be receptors in any significant ligand-receptor interactions (aggregate rank, $p < 0.05$). Genes were then filtered to include only genes that were known drug targets and were differentially upregulated by either the linear model or meta-analysis approach, resulting in a list of 483 genes with scores ranging from 1.5 to 5. Genes with scores of 3 or greater (83 genes) were manually interrogated to identify target for *in vitro* study.

In vitro drug screening and synergy experiments

Glioma cells were plated at 500 cells per well in 384 well ultra-low attachment plates (S-Bio, cat. MS-9384UZ) in 50μL of media and allowed to form spheroids overnight. Plated cells were subsequently treated with pharmacological compounds in duplicate. Compounds (Table S19) were added as 20μL of a 3.5x working solution for each drug/dilution. Drug concentrations were selected based on prior literature characterizing these compounds in cell line models. Cellular proliferation and viability were monitored via Incucyte Live Imaging technology with imaging up to every 4–6 h over 3 days. For cell death analysis we used the Cytotox green dye (1:4000 final dilution, Sartorius, cat. 4633), which stains dead cells fluorescent green and Caspase 3/7 green dye (1:1000 final dilution, Sartorius, cat. 4440 Sartorius) to specifically label those cells that are undergoing the early stages of apoptosis. Relative intensities of RFP (number live cells) or GFP (number of dying or dead cells) is determined by comparing each datapoint to the beginning of the assay (time 0). The cell death assays were only performed in the cell lines that stably express RFP (7316–1763, 7316–1769, 7316–3058, 7316–913, 7316–1746) because GFP expression would conflict with the Cytotox and Caspase dyes. Data is represented as mean ± standard error of the mean (SEM). Data were manually inspected, and erroneous fluorescent measurements due to off-center images were removed. IC_{50} values were calculated for selected drugs using Prism v10.3.1. For synergy experiments, data were represented as a percentage of cell quantity relative to the 0 timepoint DMSO condition, and analyzed using SynergyFinder[128] v3.14. Values above 100% were truncated at 100%. The Zero Interaction Potency (ZIP) score was used to identify synergistic and antagonistic interactions.

Radiation treatment and transcriptomic analysis of *in vitro* cell lines

Pediatric high-grade glioma cell lines 7316–195, 7316–1763, and 7316–1746 were plated at a density of 1 million cells per 10 cm dish. The cells were irradiated with 4 Gy of ionizing X-ray irradiation using the Precision X-ray X-RAD 320 with the default parameters of 320 kV, 12.5 mA and a 2 mm Aluminum filter. The cells were allowed to recover for 4 weeks and with regular passaging. Cell pellets were collected, and mRNA was extracted and sequenced by GeneWiz. Analysis of individual cell lines was conducted using DESeq2,[129] and a pre-ranked GSEA was conducted using the differential expression statistic for each gene. A generalized linear mixed model approach was used to aggregate results across cell lines analogous to the method used for the patient data. Briefly, a counts per million (CPM) threshold of 1 was used to call genes as expressed or not expressed, and a gene was only kept if it met this threshold in at least 3 samples. Radiation treatment (4 Gy versus 0 Gy control) was treated as a fixed effect and cell line was treated as a random effect, and a pre-ranked GSEA was conducted using the logFC for each gene.

Deconvolution of bulk RNA-sequencing data

Bulk RNA-seq expression data were downloaded from the OpenPedCan repository[37] on CAVATICA which includes updated Pediatric Brain Tumor Atlas (PBTA) data. Data were downloaded as collapsed gene expression quantification matrices in transcripts per million (TPM) along with accompanying clinical and diagnostic data for molecular subtype classification. For the analysis of subtypes, only the initial diagnostic samples were used, and when multiple samples were present for a particular patient, only one was selected. High-grade glioma included all grade 3 and 4 tumors including DIPG, DMG, and DHG. Infant-type gliomas were excluded from the analysis. Bulk RNA-seq PBTA samples were then deconvoluted using CIBERSORTx.[97] Our scRNA-Seq data annotated with neoplastic cell states and normal cell types was used as a reference for deconvolution. The reference populations included the known normal cell types established in Figure 1: mature oligodendrocytes, mature neurons, T cells, myeloid cells, vascular cells (i.e., combined endothelial cells and pericytes) and the neoplastic cell states established in Figure 2. CIBERSORTx was run with "S-mode" batch correction to make the single cell gene expression signature more closely resemble the bulk RNA-seq data. In CIBERSORTx, predicted cell abundances are converted to proportions such that they sum to unity. For the deconvolution of the cell line bulk RNA-seq data, a reference was constructed using only the neoplastic cell states, and CIBERSORTx was run with the same parameters as above.

QUANTIFICATION AND STATISTICAL ANALYSIS

No statistical method was used to predetermine sample size. All available longitudinal specimens at the Children's Hospital of Philadelphia meeting the inclusion criteria were profiled, and all data meeting standard QC thresholds were included. The Investigators were not blinded to allocation during genomics profiling and assessment of patient data. Randomization and blinding were used for all *in vitro* experiments. The two-sided Wilcoxon signed-rank test for paired samples was used to compare percentages of cell initial resection and post-therapy specimens unless otherwise specified. As the Wilcoxon test is non-parametric, we did not formally test for normality of the data. The Fisher's exact test was used to assess for recurring copy number alterations in the tumor subclone analysis, and a hypergeometric test was used to assess cell type enrichment in spatial neighborhoods. Both were adjusted for multiple hypothesis testing via the Benjamini-Hochberg method. The Wilcoxon rank-sum test was used to identify differentially expressed genes and differentially accessible transcription factor motifs and adjusted using the Bonferroni correction. Distance analysis in CODEX data was conducted using a one-sided permutation test. In all cases, boxplots indicate median value, hinges mark the 25th and 75th percentiles, and whiskers extend 1.5 times the interquartile range.